



HAL
open science

Magma storage and degassing beneath the youngest volcanoes of the Massif Central (France): Lessons for the monitoring of a dormant volcanic province

Guillaume Boudoire, G. Padeloup, Federica Schiavi, Nicolas Cluzel, Victoria Rafflin, F. Grassa, G. Giuffrida, M. Liuzzo, Andrew Harris, Didier Laporte, et al.

► To cite this version:

Guillaume Boudoire, G. Padeloup, Federica Schiavi, Nicolas Cluzel, Victoria Rafflin, et al.. Magma storage and degassing beneath the youngest volcanoes of the Massif Central (France): Lessons for the monitoring of a dormant volcanic province. *Chemical Geology*, 2023, 634, pp.121603. 10.1016/j.chemgeo.2023.121603 . hal-04257727

HAL Id: hal-04257727

<https://uca.hal.science/hal-04257727v1>

Submitted on 25 Oct 2023

HAL is a multi-disciplinary open access archive for the deposit and dissemination of scientific research documents, whether they are published or not. The documents may come from teaching and research institutions in France or abroad, or from public or private research centers.

L'archive ouverte pluridisciplinaire **HAL**, est destinée au dépôt et à la diffusion de documents scientifiques de niveau recherche, publiés ou non, émanant des établissements d'enseignement et de recherche français ou étrangers, des laboratoires publics ou privés.

Magma storage and degassing beneath the youngest volcanoes of the Massif Central (France): lessons for the monitoring of a dormant volcanic province

G. Boudoire^{1,2*}, G. Padeloup¹, F. Schiavi¹, N. Cluzel¹, V. Rafflin¹, F. Grassa², G. Giuffrida³, M. Liuzzo^{2,4}, A. Harris¹, D. Laporte¹, A.L. Rizzo^{5,6}

¹UCA, CNRS, IRD, OPGC, Laboratoire Magmas et Volcans, 6 avenue Blaise Pascal, 63178 Aubière, France

²Istituto Nazionale di Geofisica e Vulcanologia, Sezione di Palermo, 90146 Palermo, Italy

³Istituto Nazionale di Geofisica e Vulcanologia, Sezione di Catania, 95125 Catania, Italy

⁴Dipartimento di Fisica e Scienze della Terra, Università di Ferrara, 44122 Ferrara, Italy

⁵Istituto Nazionale di Geofisica e Vulcanologia, Sezione di Milano, 20133 Milano, Italy

⁶Dipartimento di Scienze dell'Ambiente e della Terra, Università di Milano Bicocca, 20126 Milano, Italy

* Corresponding author. Present address : Laboratoire Magmas et Volcans, Campus universitaire des Cézeaux, 6 Avenue Blaise Pascal, 63170 Aubière, France. Telephone: +33 (0)4 73 34 67 23. E-mail: guillaume.boudoire@uca.fr.

Abstract

Developing appropriate monitoring strategies in long-quiescent volcanic provinces is challenging due to the rarity of recordable geochemical and geophysical signals and the lack of experienced eruptive phenomenology in living memory. This is the case in the Massif Central (France) where the last eruptive sequence formed the Pavin's Group of Volcanoes, about 7 ka ago. There, current evidence of a mantle activity reminiscence is suggested by the presence of mineral springwaters, mofettes, and soil degassing. It appears fundamental as a prerequisite to decipher the evolution of the gas phase in the magmatic system at the time of the eruptive activity to understand the meaning of current local gas emissions. In this study, we develop an innovative approach coupling CO₂ densimetry and geochemistry of fluid inclusions from products erupted by the Pavin's Group of Volcanoes. 3D imagery by Raman spectroscopy revealed that carbonate forming in fluid inclusions may lead to underestimation of CO₂ density in fluid inclusions by up to 50 % and thus to unreliable barometric estimates. Fortunately, we found that this effect may be limited by focusing on fluid inclusions with a small diameter (<4 μm) and where no solid phase is detected on Raman spectra. The time evolution of the eruptions of the Pavin's Group of Volcanoes shows a progressive decrease of the pressure of magma storage (from more than 9 kbar down to 1.5-2 kbar) in parallel to magma differentiation (from basanites at Montcineyre to benmoreites at Pavin). The analysis of the noble gases entrapped in fluid inclusions yielded two main conclusions: (1) the helium isotope signature (Rc/Ra = 6.5-6.8) is in the range of values obtained in fluid inclusions from mantle xenoliths in the Massif Central (Rc/Ra = 5.6±1.1, on average) suggesting partial melting of the subcontinental lithospheric mantle, and (2) magma degassing (⁴He/⁴⁰Ar* from 4.0 to 16.2) mirrors magma differentiation and the progressive rise of the magma ponding zones of the Pavin's Group of Volcanoes. According to our modelling, about 80 % of the initial gas phase would be already exsolved from these magmas, even if stored at mantle depth. Based on the results obtained from fluid inclusions, we propose a model of the evolution of the signature of noble gases and carbon isotopes from mantle depth to crustal levels. In this frame, gas emissions currently emitted in the area (Rc/Ra = 6.1-6.7 and ⁴He/⁴⁰Ar* = 1.7) point to an origin in the lithospheric mantle. This study strongly encourages the establishment of a regular sampling of local gas emissions to detect potential geochemical variations that may reflect a change from current steady-state conditions.

Keywords

Fluid inclusions, Barometry, Noble gases, Magma degassing, Monitoring

1. Introduction

The global population growth raises severe issues about our way to live in a sustainable world and to face natural disasters. With almost one in eight people living within 100 kilometres of an active

53 volcano (Brown et al., 2015), volcanic eruptions constitute one of the main natural hazards for
54 humanity (Oppenheimer, 2015). In this regard, long-quiescent volcanic provinces play a peculiar
55 role. On the one hand, the general lack of eruptive activity in the collective memory tends to favour
56 the settling of local populations and socio-economic development on lands covered by fertile
57 volcanic soils (Shoji and Takahashi, 2002). This is even truer in Southern countries where
58 agriculture represents often one of the main economic sources and is fundamental for the survival of
59 local populations. On the other hand, long periods of quiescence may strongly favour the energy
60 accumulation at depth and drive magmas near a critical pressure point leading to violent eruptions
61 (Chiodini et al., 2016). This parallel evolution significantly increases the probability of fatal
62 eruptions, even more considering the lack of preparedness of local population in face of a natural
63 hazard with a low occurrence frequency. The development of appropriate monitoring strategies in
64 long-quiescent volcanic provinces is also challenged by (1) the rarity of signals that may indicate
65 residual magmatic activity, and (2) the difficulty of convincing decision-makers of the necessity to
66 implement a policy of prevention (rather than reaction) in face of an a priori non-imminent risk.
67 This situation applies to the French Massif Central (France), where the last known eruption is dated
68 at $6,730 \pm 170$ a BP (Juvigné and Miallier, 2016). The presence of surface manifestations of a
69 potential ‘residual’ magmatic activity is testified by the numerous mineral springs spread over the
70 territory with clear magmatic origin (Matthews et al., 1987; Bräuer et al., 2017; Moreira et al.,
71 2018), together with areas of intense soil (CO_2 -Rn) degassing (Battani et al., 2010; Gal and Gadalia,
72 2011; Gal et al., 2018). However, both types of occurrences remain poorly documented to date.
73 Although fundamental to the development of regional monitoring strategies, there is no consensus
74 on the origin of the degassing. Some studies suggest the presence of still partially molten mid-
75 crustal reservoirs beneath the area (Martel et al., 2013; France et al., 2016), while others refer to
76 fluid transport in deep reaching faults from magmatic reservoirs within the subcontinental
77 lithospheric mantle (SCLM; Bräuer et al., 2017).

78 Previous studies about noble gases from the European Cenozoic Rift System are based on
79 either natural gas emissions (Bräuer et al., 2013, 2017; Moreira et al., 2018) or fluid inclusions in
80 crystals from mantle xenoliths (Buikin et al., 2005; Gautheron et al., 2005; Rizzo et al., 2018,
81 2021). Natural gas emissions may be affected by atmospheric-crustal contamination during the
82 ascent of magmatic fluids (Barry et al., 2013) that may hide the primitive signature of the gaseous
83 component. For its part, the gas entrapped in fluid inclusions in crystals from mantle xenoliths
84 could have a different isotopic signature than the one linked to magma ascent. To overcome these
85 limitations, we aim at studying the geochemical variability (noble gases, carbon isotopes) of the gas
86 entrapped in fluid inclusions from crystals hosted in tephra erupted by the Pavin’s Group of
87 Volcanoes, i.e., the youngest volcanoes of the French Massif Central. We compare the results to the
88 composition of gas found in mantle xenoliths and surface gas emissions. In this study, we couple
89 geochemical markers to barometric estimations from fluid inclusions to decipher the evolution of
90 magmatic gases upon ascent (Boudoire et al., 2018) and discuss the origin of the gas released in the
91 area. To achieve these objectives, we use an innovative approach based on (1) the quantification of
92 the influence of carbonate precipitation on CO_2 densities in fluid inclusions to retrieve barometric
93 estimates, and (2) the first chemical characterization (for the French Massif Central if not for the
94 European Cenozoic Rift System) of the gas entrapped in fluid inclusions in phenocrysts from lavas.

96 2. Geological context and sampling strategy

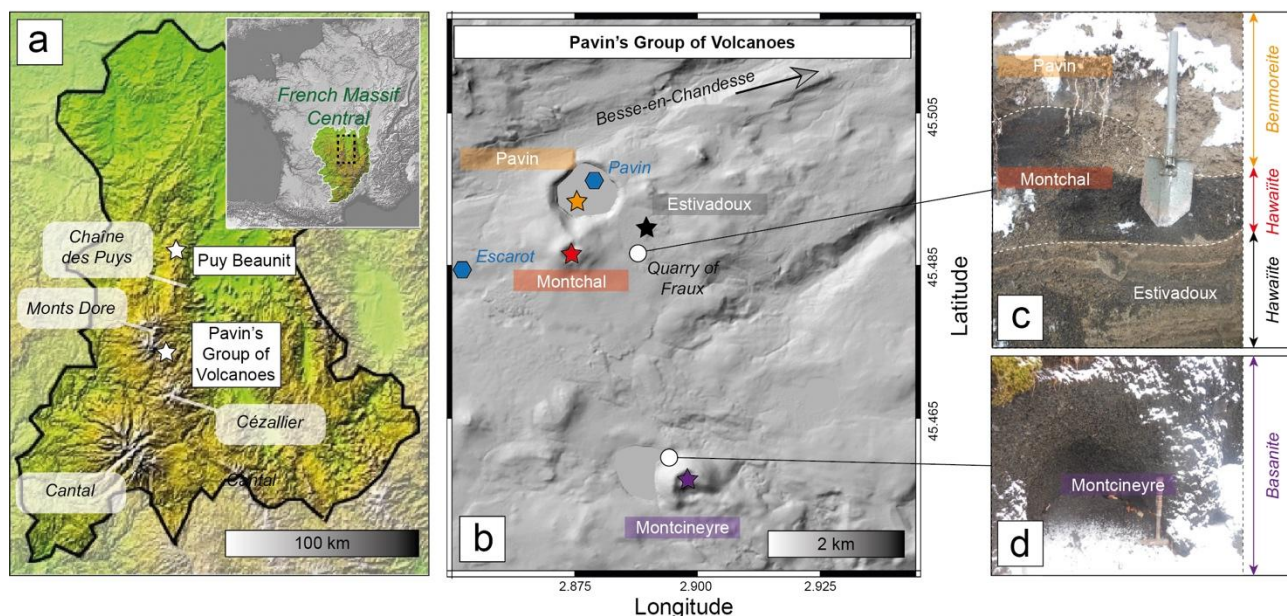
97 The Cenozoic European Volcanic Province (CEVP) was generated by intraplate alkaline volcanism
98 related to the European Cenozoic Rift System (ECRS) surrounding the Alpine orogen (Merle and
99 Michon, 2001; Lustrino and Wilson, 2007) and extending over about 1,500 km. The CEVP consists
100 of three main areas marked by volcanic activity: the French Massif Central, the Rhenish Massif, and
101 the Bohemian Massif (Ulrych et al., 1999). The youngest volcanic activity in the CEVP formed the
102 Pavin maar-crater in the French Massif Central about 7 ka ago (Fig. 1; Juvigné and Miallier, 2016).
103 However, the CEVP still presents evidence of a residual or renewed magmatic activity. The

104 province is characterised by current degassing in mineral springs, mofettes, and through the soil
105 (Bräuer et al., 2013, 2017; Gal et al., 2018; Moreira et al., 2018). Presently active magmatic
106 processes have been recognised or hypothesised during the last 20 years beneath the Cheb basin, in
107 the Bohemian Massif (Bräuer et al., 2011), and in the Eifel region, in the Rhenish Massif (Hensch et
108 al., 2019; Kreemer et al., 2020) with both local seismicity and ground deformation. In the French
109 Massif Central, petrological investigations have suggested the potential presence of one or more
110 magma reservoirs, still partially molten, beneath the Chaîne des Puys (Martel et al., 2013; France et
111 al., 2016; Boivin et al., 2017). These inferences on the current state of magmatic activity in the
112 CEVP, close to densely populated areas, may raise major concerns about civil protection and risk
113 management.

114 The French Massif Central (FMC) is the largest magmatic province of the CEVP and is
115 characterised by typical intraplate alkaline series (Michon and Merle, 2001). The Cenozoic volcanic
116 activity spread over three main periods due to local extension and mantle upwelling of the ECRS: a
117 pre-rift stage (65-34 Ma), a rifting stage (34-15 Ma), and a post-rift stage marked by major
118 magmatic events. The post-rift stage is subdivided into three phases of volcanism. The first phase
119 (9-6.3 Ma) is marked by eruptive activity in the Cantal (**Fig. 1a**), Aubrac, Velay, and Coirons. The
120 second phase (3.5-0.23 Ma) took place mainly in the Monts-Dore (**Fig. 1a**) and Devès. Finally, the
121 most recent one occurred in the Chaîne des Puys (160-6.7 ka; **Fig. 1a**) and Bas-Vivarais (Nomade
122 et al., 2016). The last known eruptive site in the FMC (the Pavin's Group of Volcanoes; 6,730±170
123 a BP; Juvigné and Miallier, 2016) is located at the southern extremity of an alignment of about 80
124 monogenetic volcanoes oriented N-S and forming the Chaîne des Puys, at the boundary between the
125 Monts-Dore and the Cézallier (**Fig. 1a**). The Pavin's Group of Volcanoes is composed of 4
126 monogenetic volcanoes that erupted over a short period of time of about 100-700 years (**Fig. 1b**;
127 Juvigné and Miallier, 2016): Montcineyre, Estivadoux, Montchal, and Pavin (from the oldest to the
128 youngest). Volcanic products from these edifices mark a clear trend of magma differentiation from
129 basanite at Montcineyre (the most primitive lavas erupted in this part of the FMC in the last 200 ka)
130 to benmoreite at Pavin (maar-diatreme volcano now filled by a meromictic lake with dissolved
131 gases in depth; Michard et al., 1994; Jézéquel et al., 2016). Very early fractionation of amphibole
132 was recognised (based on K₂O, Sc, Co, Y, Nb, Ta, and REEs contents) in the magmatic series of the
133 Pavin's Group of Volcanoes, which differs from the early fractionation of clinopyroxene identified
134 in magmas from the Chaîne des Puys (Villemant et al., 2016). In addition to the abundance of
135 dissolved gases in the monimolimnion layer of the Pavin lake (Aeschbach-Hertig et al., 1999), the
136 area is also characterised by soil CO₂ gas emissions (Gal and Gadalia, 2011; Gal et al., 2018) and
137 by degassing at the Escarot mofettes (less than 3 km away). There, the ³He/⁴He signature is the
138 most primordial ever found in the FMC and suggests direct gas migration from a magmatic
139 reservoir in the SCLM to the surface with only minor crustal contamination during the ascent
140 (Aeschbach-Hertig et al., 1999; Bräuer et al., 2017; Moreira et al., 2018).

141 In this study, fresh glassy lapilli from Montcineyre and Montchal, and pumices from Pavin
142 (outcrop of the Quarry of Fraux) were sampled (**Fig. 1c, d**). Analyses made on tephra favour the
143 preservation of fluid inclusions in host crystals (Klügel et al., 2020), limit the effect of crystal
144 recycling and the amount of xenocrysts (Boudoire et al., 2021), and cover the whole differentiation
145 trend of the magmatic series of the Pavin's Group of Volcanoes (Villemant et al., 2016). In this
146 study, one tephra sample from each eruptive site was collected and considered representative of the
147 magma involved in each eruption. This assessment is supported by the chemical, mineral, and
148 textural homogeneity of the tephra deposits from the same eruptive site along the whole
149 stratigraphic sequence (Rondet et al., 2019). In addition, two mantle enclaves from the Puy
150 Gonnard, a part of Puy Beaunit volcano, at the northernmost end of the Chaîne des Puys (**Fig. 1a**),
151 were sampled to allow the comparison between results obtained from fluid inclusions in tephra
152 phenocrysts and mantle crystals. Puy Beaunit (43,900±5,100 a BP) is well known for its exceptional
153 mantle enclave abundance and diversity (Brousse and Rudel, 1964; Féménias et al., 2001, 2004).
154 Based on textural and mineral abundance analysis of thin sections (**Fig. 2**), these mantle enclaves

155 correspond to a coarse to transitional harzburgite (**Fig. 2a, b**) and a granuloblastic lherzolite (**Fig.**
 156 **2c, d**) following the nomenclature of mantle enclaves at Puy Beaunit defined by Féménias et al.
 157 (2004). The geochemical signatures of Montcineyre basanite and Puy Beaunit melt inclusions
 158 (Jannot et al., 2005) are close enough to assume a common mantle source beneath both areas
 159 (Villemant et al., 2016). Dissolved gases were also sampled at 70 and 90 m depth in the Pavin lake
 160 together with gas emissions from the Escarot mofettes to compare the chemistry of the gas phase
 161 entrapped in fluid inclusions with that of surface gas emissions.
 162



163
 164 **Fig. 1.** (a) Location map of the French Massif Central and the Auvergne region with the two main sampled sites: Puy
 165 Beaunit (mantle enclaves) and (b) the Pavin's Group of Volcanoes (lapilli, pumices, dissolved gases in Pavin lake,
 166 Escarot mofettes) in the vicinity of the village of Besse-en-Chandesse. (c, d) Photographs of the outcrops where lapilli
 167 were sampled.
 168

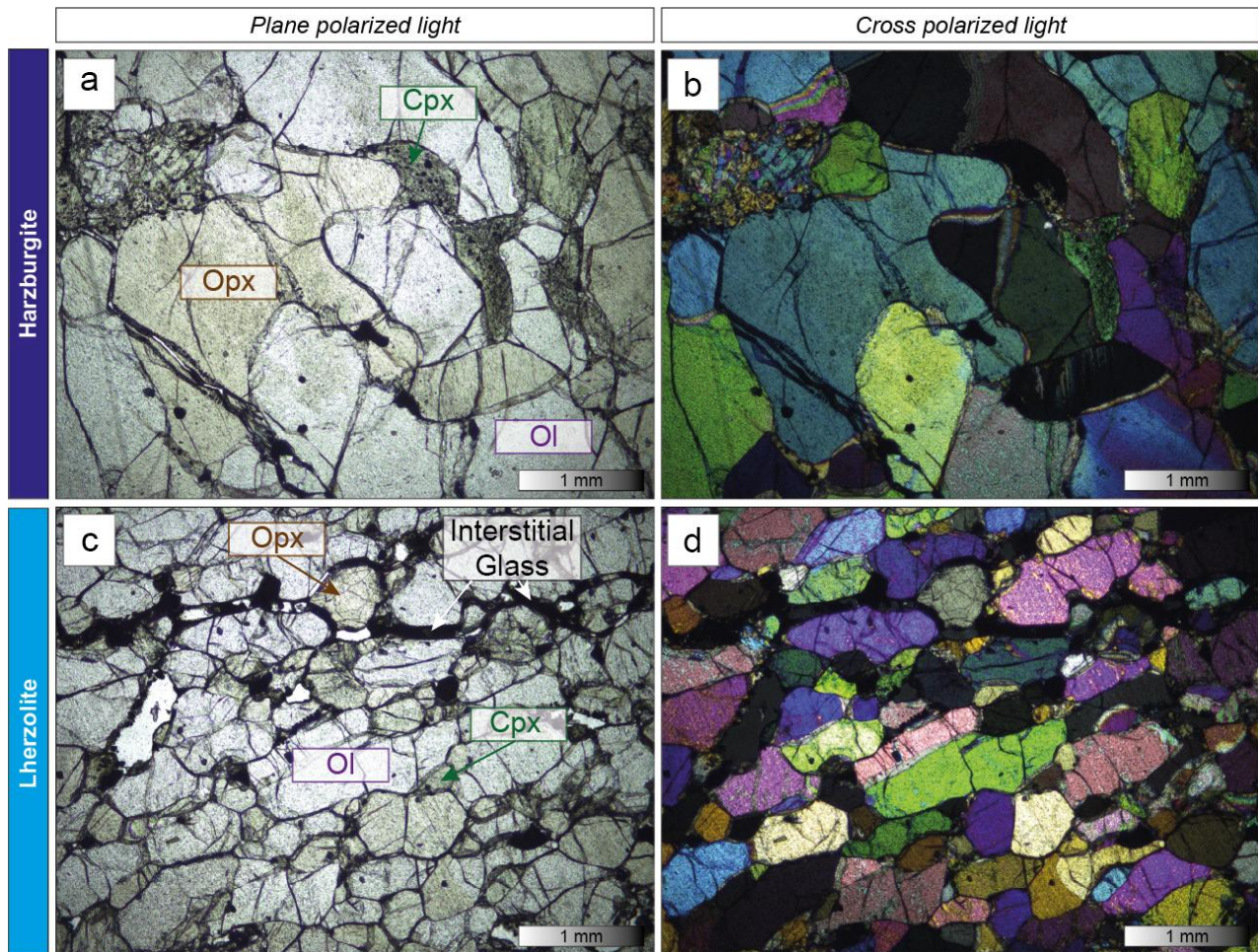


Fig. 2. Transmitted light photomicrographs (in plane and cross polarized light) of the thin sections of two mantle enclaves sampled at Puy Beaunit: (a, b) harzburgite and (c, d) lherzolite (nomenclature of ultramafic rocks from Streckeisen, 1974). Ol, olivine; Cpx, clinopyroxene; Opx, orthopyroxene.

169
170
171
172
173
174
175
176
177
178
179
180
181
182
183
184
185
186
187
188
189
190
191
192
193
194
195

3. Methodology

3.1. Crystal composition

Crystals (olivine, clinopyroxene, orthopyroxene, and amphibole) were hand-picked from crushed and sieved lapilli (Montcineyre, Montchal), pumices (Pavin) and mantle enclaves (Puy Beaunit). Electron microprobe analyses of mineral phases (**Appendix 1**) were performed using a Cameca SXFive at the Laboratoire Magmas et Volcans (Aubière, France) operated with a 15 kV accelerating voltage and a 20 nA current focused beam. Relative errors were 0.5-1.7 % (Si, Mg, Fe, Ca, Al), 16-24 % (Ti, Cr, Mn), and 62-111 % (Ni, K), on average. For olivine, the relative error on CaO was 0.5-15 %. For pyroxene, the relative error on Al₂O₃ was 0.9-3 %.

3.2. Fluid inclusions composition

The composition of the fluid inclusions (**Appendix 2**) was determined at the Laboratoire Magmas et Volcans using an inVia confocal Raman micro-spectrometer manufactured by Renishaw. The micro-spectrometer was equipped with a 532.1 ± 0.3 nm diode-pulsed solid state laser (200 mW output power), a Peltier-cooled CCD detector of 1040 x 256 pixels, a Rayleigh rejection edge filter, and a Leica DM 2500 M optical microscope with a motorised XYZ stage. Laser power was periodically checked and reduced to 19 mW on the sample surface. A 100x microscope objective, a 20 μ m slit aperture, and a grating of 2400 grooves/mm were used leading to a spectral resolution better than 0.4 cm^{-1} and spatial resolutions of 1 μ m (horizontal), and 2-3 μ m (vertical) near the

196 surface. Calibration of peak positions was performed based on the 520.5 cm⁻¹ peak of Si and the
 197 1331.5 cm⁻¹ peak of diamond. The spectra were recorded with the WiRE™ 4.2 software in a single
 198 window collection (recommended by Lamadrid et al., 2017, for CO₂ densimetry) of 365-1575 cm⁻¹
 199 to cover the vibrational frequencies of mineral phases (host crystals, carbonates, sulphates) and
 200 gaseous phases (CO₂-SO₂). Extended spectra were recorded for each family of fluid inclusions (and
 201 for each sample) in the wavenumber range 60-4500 cm⁻¹ to investigate the presence of other
 202 mineral (sulphides) and fluid phases (H₂O and/or OH molecules). Acquisition time for a single
 203 analysis was fixed at 60 s and room temperature was kept at ~20.5 °C.

204 He (³He, ⁴He), Ne (²⁰Ne), Ar (⁴⁰Ar, ³⁸Ar, ³⁶Ar), C (¹³C/¹²C noted as δ¹³C versus VPDB
 205 reference in per mil) isotopes were measured at the Istituto Nazionale di Geofisica e Vulcanologia
 206 (INGV), Sezione di Palermo (Italy). Measurements were performed either in the gas phase
 207 entrapped in fluid inclusions hosted in minerals or in surface gas emissions, with small differences
 208 in the gas extraction or introduction method as well as in the mass spectrometers used for the
 209 analysis. In detail, 0.4-1.2 g of crystals (among olivine, clinopyroxene, orthopyroxene, and
 210 amphibole) were hand-picked for noble gas measurements, while 0.5-3.1 g of orthopyroxene were
 211 used for CO₂ extraction and carbon isotope measurements. Residual glass around the crystals was
 212 removed using fluoroboric acid. Then, crystals were cleaned in an ultrasonic bath and loaded in two
 213 distinct single-step crushers for the noble gas and CO₂ extraction from fluid inclusions, following
 214 the protocols reported in Rizzo et al. (2018, 2021) and Sandoval-Velasquez et al. (2022). After
 215 purification and separation of distinct species with cryogenic techniques, He and Ne isotopes were
 216 analysed using two distinct split-flight-tube mass spectrometers (Helix SFT-Thermo), and Ar
 217 isotopes using a multi-collector mass spectrometer (Argus, GVI). Typical blanks for He, Ne, and Ar
 218 were <10⁻¹⁵, <10⁻¹⁶, and <10⁻¹⁴ mol, respectively. The analytical uncertainties (1σ) for ³He/⁴He are
 219 <2.4 %. The ¹³C/¹²C was measured using a Thermo (Finnigan) Delta Plus XP CF-IRMS connected
 220 to a Trace GC gas chromatograph and a Thermo (Finnigan) GC/C III interface. The absolute δ¹³C
 221 analytical error is <0.4 ‰ (1σ).

222 In the case of surface gas emission samples, an aliquot of gas was introduced in three
 223 distinct calibrated pipettes of 0.1 cm³ each and expanded in three distinct ultra-high-vacuum
 224 purification lines dedicated to He, Ne and Ar. After purification procedures, He was introduced in a
 225 Helix SFT-GVI, Ne in a Helix MC Plus-Thermo, Ar in a Helix MC-GVI for the respective isotopic
 226 measurements, following the purification and analytical protocols reported in Rizzo et al. (2021).
 227 Measured ³He/⁴He were corrected for atmospheric contamination based on their ⁴He/²⁰Ne and the
 228 values are expressed as Rc/Ra (Ra = ³He/⁴He in air) with:

$$R_c = \frac{(R_m \times ({}^4\text{He}/{}_{20}\text{Ne})_m - R_a \times ({}^4\text{He}/{}_{20}\text{Ne})_a)}{(({}^4\text{He}/{}_{20}\text{Ne})_m - ({}^4\text{He}/{}_{20}\text{Ne})_a)}$$

230 where R_m and (⁴He/²⁰Ne)_m are the measured values, and R_a and (⁴He/²⁰Ne)_a refers to the
 231 atmospheric value (0.318; Ozima and Podosek, 2002). ⁴⁰Ar was also corrected for the atmospheric
 232 contamination, as follows:

$${}^{40}\text{Ar}^* = {}^{40}\text{Ar}_m - ({}^{36}\text{Ar}_m \times ({}^{40}\text{Ar}/{}^{36}\text{Ar})_a)$$

234 where ⁴⁰Ar* is the corrected value, ⁴⁰Ar_m the measured value, and (⁴⁰Ar/³⁶Ar)_a = 298.56 (Lee et al.,
 235 2006).
 236
 237

238 3.3. 3D imagery of fluid inclusions

239 Raman tomography was performed on three fluid inclusions using <5 mW laser power.
 240 Acquisitions were collected with a sampling step distance of 0.5-1 μm in the horizontal plane and 1-
 241 1.5 μm along the vertical axis, and 10-15 s/point. For each fluid inclusion, 3D mapping produced a

242 single hypermap of ten to fifteen thousand spectra in the XYZ space. The WiRE™ 4.2 software was
243 used to collect, process, and view 3D volume data, allowing spectral information to be analysed in
244 all dimensions simultaneously. Data processing consisted of several steps. First, narrow random
245 peaks known as cosmic rays were identified and removed from the datasets. Second, the baseline
246 was subtracted from the spectra by fitting the most appropriate polynomial function that passes
247 through anchor points in peak-free spectral regions. After an initial overview of the inclusion
248 volume to recognise the phases present, a representative, well distinct peak, generally
249 corresponding to the strongest vibrational mode, was selected for each phase. A 3D distribution
250 map of the peak intensity was created using the ‘signal to baseline’ parameter to calculate the area
251 under the selected peak. The volume occupied by each phase was defined by setting a threshold of
252 intensity of the selected peak. To precisely delineate the volume of a phase, horizontal and vertical
253 variations in peak intensity were carefully analysed, since Raman signal intensity decreases quite
254 rapidly at mineral rims. Volume reconstruction of the inclusion was obtained by merging the 3D
255 maps of all phases into a combined 3D representation on which different phases are identified by
256 different colors. Finally, the recovered volume fraction of each phase was converted to a mass value
257 using the appropriate density. Total CO₂ mass was obtained by adding the mass of fluid CO₂ and
258 that of CO₂ stored in carbonates. Uncertainties in volume reconstruction from Raman tomography
259 are mainly due to the vertical spatial resolution of the technique that can be larger than the size of
260 minerals within the inclusions, resulting in aggregates of very small crystals being represented as
261 large continuous masses. The volumetric reconstruction and associated uncertainties are therefore
262 very sensitive to the intensity threshold defined for data processing. For additional details about the
263 procedure followed for acquisition and processing of 3D maps, and associated uncertainties as well,
264 the reader is referred to Schiavi et al. (2020).

265

266 **3.4. Barometry based on CO₂ density in fluid inclusions**

267 CO₂ density was calculated from the Fermi dyad split (Δ ; Van den Kerkhof and Olsen, 1990;
268 Frezzotti et al., 2012) between the 1388 and 1285 cm⁻¹ peaks (Boudoire et al., 2021). The linearity
269 of the spectrometer was tested by the use of a diamond standard (peak at 1331.5 cm⁻¹). Corrected
270 splitting of the CO₂ Fermi dyad was then determined following the expression (1) of Lamadrid et al.
271 (2017). Using the corrected instead of the measured splitting of the Fermi dyad has a negligible
272 effect on the calculated CO₂ density (<0.01 g/cm³). Precautions were taken during the crystal
273 preparation to get homogeneous host crystal radius (around 1 mm) together with limited crystal
274 thickness (between 200 and 400 μ m) to reduce the variability of temperatures in fluid inclusions
275 induced by laser heating (Hagiwara et al., 2021a). Based on the equation of Hagiwara et al. (2021b),
276 we estimated a maximum temperature of 42.6 °C for fluid inclusions investigated in this study. For
277 Δ between 102.85 and 105 cm⁻¹, this value of 42.6 °C leads to a maximum uncertainty on CO₂
278 density of 0.038 g/cm³ with respect to room temperature by using the equations of Sublett et al.
279 (2020). This part of the uncertainty related to temperature is called hereafter ϵ (temperature). If we
280 recognise that the use of Raman spectroscopy at room temperature for the evaluation of CO₂ density
281 in fluid inclusions is not applicable between 0.22 and 0.74 g/cm³ (coexistence of gas and liquid
282 CO₂), we highlight that, in this study: (i) only 10 fluid inclusions fall in this CO₂ density range (for
283 a total of 70 fluid inclusions) and (ii) laser heating using a 19 mW power on the sample is expected
284 to rise the temperature of fluid inclusions above the critical temperature of CO₂ (31 °C; Hagiwara et
285 al. 2021a). Consistently, no moving CO₂ vapour bubble was detected in these fluid inclusions
286 immediately after the analysis arguing for the presence of a homogeneous CO₂ phase during the
287 analysis. Three Raman spectra were acquired for each fluid inclusion to test the reproducibility of
288 the analyses. If the CO₂ densities estimated from these three Raman spectra differed by more than
289 0.05 g/cm³, the fluid inclusion was discarded from the dataset. In this way, the cases of two-phase
290 gas-liquid mixture can also be identified. In the absence of calibrated curves for our instrument
291 (Lamadrid et al., 2017), we tested the reliability of the experimental equations of Song et al. (2009),
292 Fall et al. (2011), Wang et al. (2011) and Lamadrid et al. (2017) on a set of 4 pure CO₂ fluid

293 inclusions (0.60-0.92 g/cm³ of CO₂ determined by microthermometry) used as internal standards.
 294 The equation of Song et al. (2009) provided the most reliable results with a deviation, $\varepsilon(\text{analytical})$,
 295 not exceeding 0.037 g/cm³ of CO₂, and was used in this study. Finally, the total uncertainty,
 296 $\varepsilon(\text{TOT})$, on CO₂ density related to the use of the CO₂ densimeter of Song et al. (2009) and to the
 297 analysis of fluid inclusions is (Boudoire et al., 2021):
 298

$$\varepsilon(\text{TOT}) = \sqrt{\varepsilon(\text{analytical})^2 + \varepsilon(\text{temperature})^2 + \varepsilon(\text{processing})^2}$$

299
 300 where $\varepsilon(\text{processing})$ is the uncertainty related to the spectral resolution by peak fitting (<0.014
 301 g/cm³; Kobayashi et al., 2012). In this study $\varepsilon(\text{TOT})$ is equal to 0.054 g/cm³, which corresponds to a
 302 maximum uncertainty of 70 MPa, following the procedure described below. Rare sulphates,
 303 sulphides, carbonates, and either liquid or vapour water were sometimes detected in a few fluid
 304 inclusions. This observation points to the presence of a CO₂-H₂O initial mixture (Boudoire et al.,
 305 2018, 2021). In agreement with previous inferences made on CO₂-H₂O initial mixture in fluid
 306 inclusions analysed in other similar studies (Hansteen and Klügel, 2008; Zanon and Frezzotti,
 307 2013), we consider an upper limit of 10% mol of H₂O in the initial exsolved phase. Such a value
 308 leads to a maximum increase of density of 0.03 g/cm³. Pressure was estimated with the ISOC code
 309 (Bakker, 2003) using the equation of state of Duan et al. (1992, 1996) set for CO₂-H₂O mixture on a
 310 large range of pressure and temperature. Based on the composition of the lavas (Villemant et al.,
 311 2016) and the MgO-thermometer of Putirka (2008), the temperature was fixed at 1300 °C, 1200 °C,
 312 and 1050 °C for the basanite of Montcineyre, the hawaiiite of Montchal, and the benmoreite of
 313 Pavin. Previous estimations made for the benmoreitic magma of Pavin are in the range 950-975 °C
 314 (Rondet et al., 2019). Any uncertainty on temperature results only in minor errors on pressure (<50
 315 MPa for a shift of 100 °C). Following the results obtained by Féménias et al. (2001) on mantle
 316 enclaves at Puy Beaunit, the temperature was fixed at 850 °C and 1000 °C for granuloblastic
 317 lherzolite and transitional harzburgite, respectively. Finally, the cumulated uncertainty on pressure
 318 estimates from CO₂ densimetry in fluid inclusions does not exceed 90 MPa in this study.
 319
 320

321 4. Results

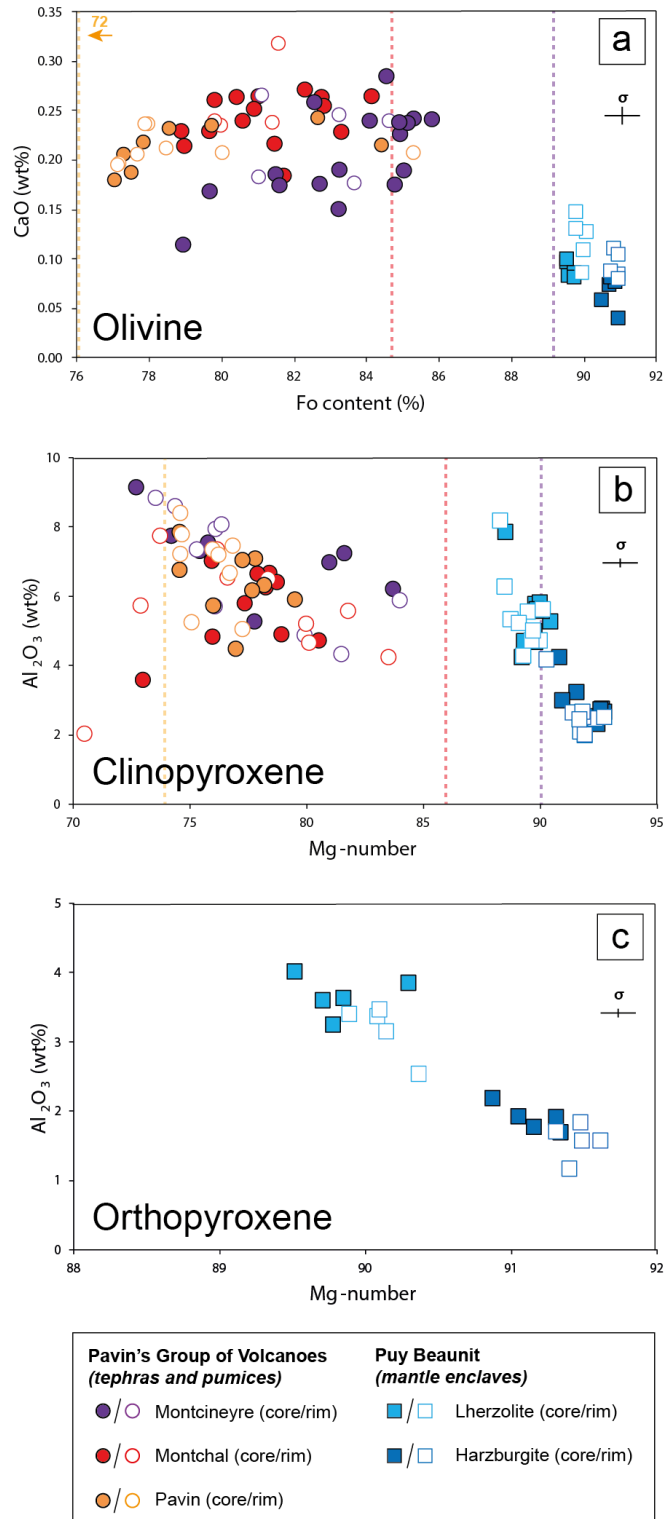
322 4.1. Mineralogy

323 The compositions of olivine crystals from the lapilli and pumices of the three volcanoes largely
 324 overlap (**Fig. 3a**): from Fo_{78.9} to Fo_{85.8} at Montcineyre, from Fo_{78.9} to Fo_{84.1} at Montchal, and from
 325 Fo_{77.1} to Fo_{85.3} at Pavin. Meanwhile, the average forsterite (Fo) content of olivine crystals slightly
 326 decreases from Montcineyre (Fo_{83.2}) to Montchal (Fo_{81.1}) and Pavin (Fo_{79.1}) products. Noteworthy,
 327 part of olivine crystals from Montcineyre show a lower CaO content (0.12-0.19 wt%) than that from
 328 Montchal and Pavin (0.18-0.36 wt%) at constant forsterite content (**Fig. 3a**). The Mg-numbers
 329 (Mg#) of olivine crystals from lapilli and pumices differ from those of olivine crystals at
 330 equilibrium with the bulk rock: they are lower at Montcineyre and Montchal, and higher at Pavin
 331 (**Fig. 3a**). Both normal and reverse zoning is observed in olivine crystals from Montcineyre and
 332 Pavin, whereas only normal zoning was identified in the few analysed olivine crystals from
 333 Montchal (**Table 1**). The range of composition of olivine crystals from mantle enclaves is narrow
 334 (**Fig. 3a**): from Fo_{89.5} to Fo_{90.1} for the lherzolite and from Fo_{90.5} to Fo_{91.0} for the harzburgite. In both
 335 enclaves, an increase of the CaO content at constant forsterite content is observed from crystal core
 336 to rim.

337 As in the case of olivine, the compositions of clinopyroxene crystals from the lapilli and
 338 pumices of the three volcanoes overlap widely (**Fig. 3b**): the Mg-number ranges from 72.7 to 84.0
 339 at Montcineyre, from 70.5 to 83.5 at Montchal, and from 74.5 to 79.5 at Pavin. The decrease of the
 340 Mg-number of clinopyroxene crystals is coupled with a decrease in SiO₂ and CaO contents and with
 341 an increase in Al₂O₃, TiO₂, and Na₂O contents, which mirror the behaviour described for
 342 clinopyroxene crystals from mantle enclaves. A few clinopyroxene crystals from Montcineyre

343 display the highest Mg-numbers together with an enrichment in Al₂O₃ and TiO₂ contents. In the
344 same way as for olivine crystals, the Mg-numbers of clinopyroxene crystals from lapilli and
345 pumices differ from the Mg# computed for clinopyroxene at equilibrium with the bulk rock: they
346 are lower at Montcineyre and Montchal, and higher at Pavin (**Fig. 3b**). Complex normal and reverse
347 zoning is observed in clinopyroxene crystals from all lapilli and pumices, whatever the eruptive site
348 (**Table 1**). Clinopyroxene crystals are mainly diopside in both mantle enclaves, lapilli, and pumices.
349 In mantle enclaves, the Mg-number of clinopyroxene crystals decreases (as well as SiO₂ and CaO
350 contents) from harzburgite (Mg# = 91.9±0.7) to lherzolite (Mg# = 89.5±0.6) together with an
351 increase in Al₂O₃ and Na₂O contents (**Fig. 3b, Appendix 1**). No compositional zoning is observed
352 from crystal core to rim.

353 Orthopyroxene crystals were found only in mantle enclaves. The Mg-number decreases (as
354 well as SiO₂ content) from harzburgite (Mg# = 91.3±0.2) to lherzolite (Mg# = 90.0±0.3) together
355 with an increase in Al₂O₃ and CaO contents. A clear reverse zoning is systematically observed in
356 crystals from both harzburgite and lherzolite (**Fig. 3c**). Amphibole crystals in the pumices of Pavin
357 are kaersutite (Leake et al., 1997).
358



359
 360
 361
 362
 363
 364
 365
 366
 367
 368
 369
 370

Fig. 3. Composition of (a) olivine, (b) clinopyroxene, and (c) orthopyroxene crystals from mantle enclaves (Puy Beaunit) and tephra and pumices (Pavin's Group of Volcanoes). Dashed lines represent the compositions of olivine and clinopyroxene at equilibrium with the bulk rock (Villemant et al., 2016): in purple for Montcineyre (sample P13-8), in red for Montchal (sample P13-4), and in orange for Pavin (sample KBP3b*). For the calculations, the Fe-Mg distribution coefficients between melt and crystals (K_D) were set at 0.30 and 0.27 for olivine and clinopyroxene, respectively (Putirka, 2008). Fo represents the forsterite content of olivine crystals ($Fo = 100 \times \frac{Mg^{2+}}{Mg^{2+} + Fe^{2+} + Ca^{2+}}$) and Mg# is the Mg-number of other crystals ($Mg\# = 100 \times \frac{Mg^{2+}}{Mg^{2+} + Fe^{2+}}$).

371 **4.2. Fluid inclusions**

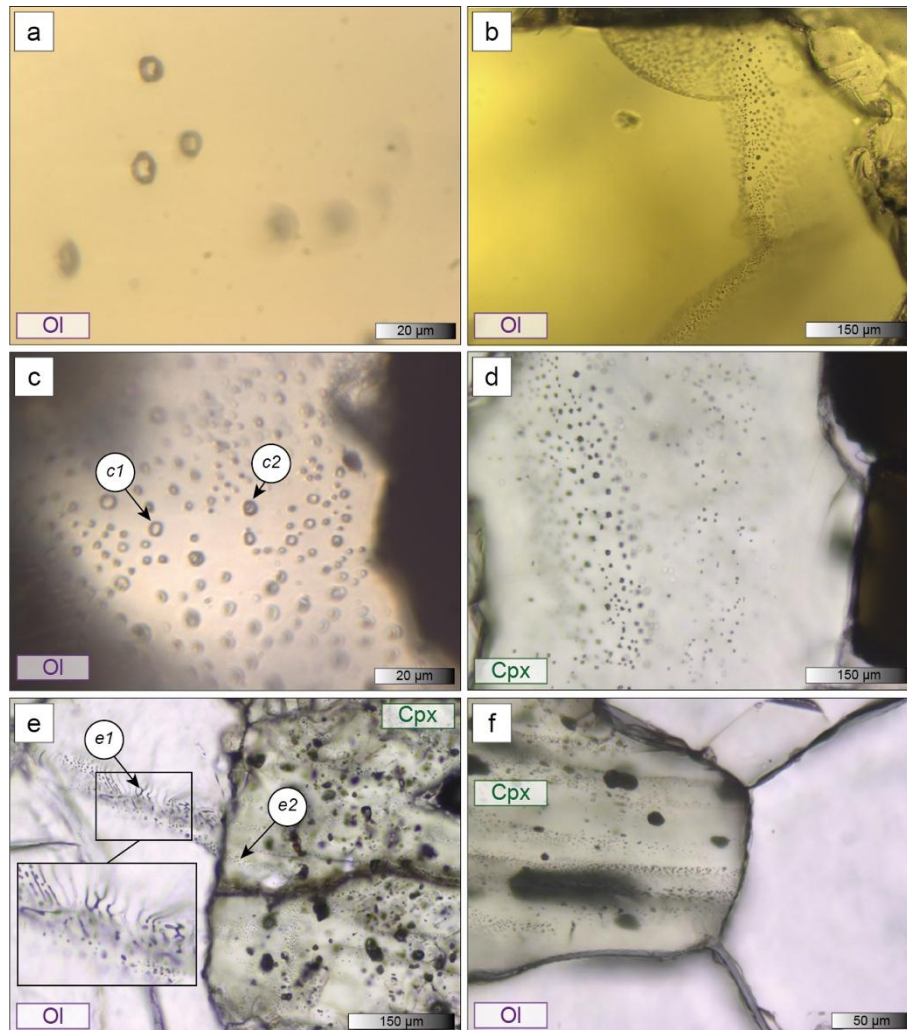
372 For lapilli and pumices of the Pavin's Group of Volcanoes, fluid inclusions were essentially
373 observed in olivine and clinopyroxene crystals. Five families of fluid inclusions were distinguished
374 (**Table 2**): (*F1*) rare primary negatively-shaped fluid inclusions with a homogeneous trapping (**Fig.**
375 **4a**), (*F2*) rare pseudo-secondary rounded fluid inclusions with a homogeneous trapping, (*F3*) trails
376 of secondary rounded fluid inclusions with a homogeneous trapping (**Fig. 4b**), (*F4*) primary
377 rounded fluid inclusions with a heterogeneous trapping characterised by the presence of either a
378 single phase or a mixture of liquid-vapour phases and, (*F5*) trails of secondary rounded fluid
379 inclusions with a heterogeneous trapping (**Fig. 4c**). All fluid inclusions are CO₂-rich. Water vapour
380 (3640 cm⁻¹ Raman peak) or a thin film of liquid water on the wall of fluid inclusions (3250-3550
381 cm⁻¹ Raman band; Frezzotti et al., 2012) were sometimes detected. Additionally, traces of SO₂ (*F1*-
382 *F5*), carbonates (mainly (Fe-)magnesite and minor Mg-calcite, *F2-F3-F5*), and sulphides (mainly
383 chalcopyrite-pyrite, *F5*) were sometimes detected by Raman spectroscopy (**Appendix 2**).

384 For mantle enclaves at Puy Beaunit, fluid inclusions were observed in olivine,
385 clinopyroxene, and orthopyroxene crystals. Four families of fluid inclusions were identified (**Table**
386 **2**): (*f1*) trails of secondary negatively-shaped fluid inclusions with a homogeneous trapping (**Fig.**
387 **4d**), (*f2*) trails of secondary necking down fluid inclusions (**Fig. 4e**), (*f3*) trails of secondary rounded
388 fluid inclusions with a homogeneous trapping (**Fig. 4f**), and (*f4*) trails of secondary rounded fluid
389 inclusions with a heterogeneous trapping. Independently of the family of fluid inclusions, those in
390 crystals from the harzburgite show traces of SO₂ (*f2-f3-f4*). Few crystals from the lherzolite show
391 traces of sulphate (mainly anhydrite and possibly kieserite, *f3*) and carbonate (dolomite, *f3*). Few
392 crystals from the harzburgite show traces of carbonate (mainly dolomite, *f3*) and sulphate
393 (anhydrite, *f3*). Viewable fluid inclusions are abundant in clinopyroxene or orthopyroxene crystals.
394 For the harzburgite, trails of secondary rounded fluid inclusions present in clinopyroxene or
395 orthopyroxene crystals either (1) take a necking down shape (**Fig. 4e**) or (2) are not viewable
396 anymore in adjacent olivine crystals (**Fig. 4f**).

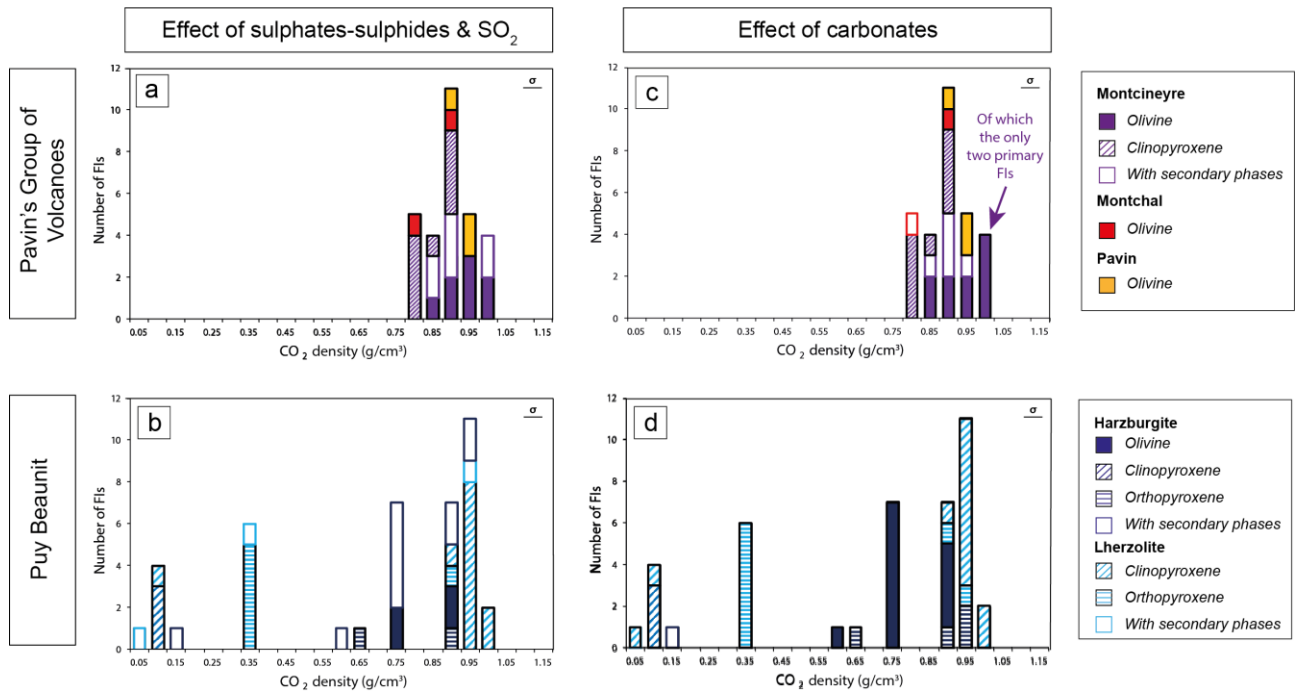
397 For lapilli and pumices of the Pavin's Group of Volcanoes, the CO₂ density (ρ) in fluid
398 inclusions is systematically higher than 0.83 g/cm³. The maximum CO₂ density decreases from
399 Montcineyre ($\rho_{\max} = 1.04$ g/cm³) to Pavin ($\rho_{\max} = 0.98$ g/cm³) and Montchal ($\rho_{\max} = 0.91$ g/cm³).
400 For mantle enclaves at Puy Beaunit, the CO₂ density in fluid inclusions covers a larger range of
401 values (from 0.08 to 1.01 g/cm³) without clear distinction between harzburgite ($\rho_{\max} = 0.97$ g/cm³)
402 and lherzolite ($\rho_{\max} = 1.01$ g/cm³). Leaving aside the very low-density values, this range of CO₂
403 density is close to that reported by Bilal and Touret (1977) for catazonal xenoliths from the Bournac
404 volcano in the FMC (0.72 – 1.08 g/cm³). Differences in CO₂ density (average, maximum) among
405 fluid inclusions are noteworthy between (1) primary and secondary/pseudo-secondary fluid
406 inclusions, (2) families of fluid inclusions in each sample, and (3) hosting mineral phases, such as
407 olivine vs. clinopyroxene (**Table 2, Fig. 5**). This phenomenon was extensively documented in other
408 studies focused on fluid inclusions (Hansteen and Klügel, 2008, for a review). These density
409 differences may be related to the history of fluid inclusion entrapment during crystal growth
410 (Hansteen and Klügel, 2008) and/or distinct re-equilibration effects depending on the crystal lattice
411 (Hildner et al., 2011).

412 Additionally, the effect of the presence of secondary phases in fluid inclusions on CO₂
413 density was qualitatively evaluated (**Fig. 5, Appendix 2**). No significative difference is observed
414 between pure CO₂-rich fluid inclusions and those characterised by the presence of sulphates or SO₂
415 (with a low intensity Raman peak at 1148-1150 cm⁻¹) (**Fig. 5a, b**). This is consistent with previous
416 inferences noting that small amounts of additional components in CO₂-dominated fluid inclusions
417 do not affect the interpretation of the trapping conditions (Van den Kerkhof and Olsen, 1990;
418 Frezzotti et al., 2012). Conversely, we suspect a potential role of carbonate precipitation in the
419 decrease of the CO₂ density in some fluid inclusions belonging to the same family (**Fig. 5c, d**). For
420 instance, the CO₂ density of the *F5* family in Montcineyre crystals decreases from 1.00 g/cm³ in
421 fluid inclusions without carbonates to 0.88-0.91 g/cm³ in fluid inclusions with carbonates. 3D

422 Raman imaging confirmed the presence of accessory carbonate, sulphide, and/or sulphate in some
 423 fluid inclusions, especially in the largest ones (**Fig. 6**). Hematite was detected in a large fluid
 424 inclusion (**Fig. 6a**). Within a same trail of secondary fluid inclusions in olivine crystals from
 425 Montcineyre, the CO₂ density decreases from 1.00 g/cm³ (FI3 without secondary phases) to 0.92
 426 g/cm³ (FI2 with carbonate and sulphide), and to 0.88 g/cm³ (FI1 with carbonate, sulphide, and
 427 hematite). This evolution also mirrors a change in the diameter of the fluid inclusions, from 3.5 to
 428 11.5 μm (**Fig. 6**). The effect of both carbonate precipitation and volume of fluid inclusions on CO₂
 429 density will be discussed in a following section.
 430

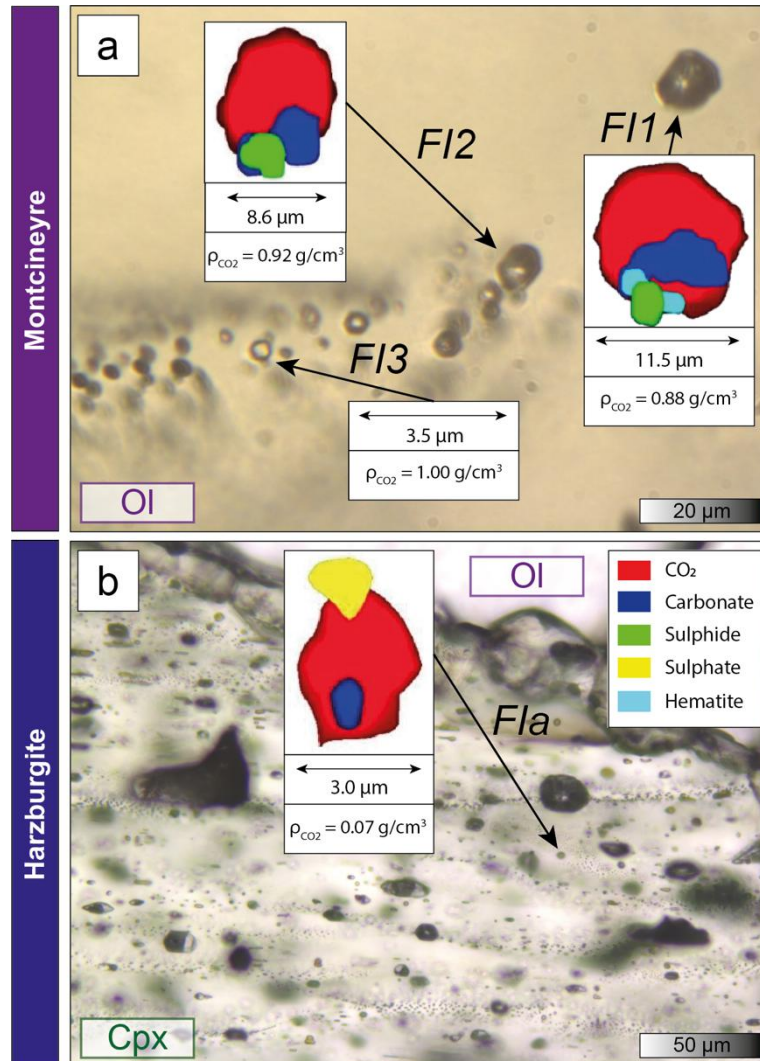


431
 432
 433 **Fig. 4.** Transmitted light photomicrographs of the families of fluid inclusions (see text for explanations) in crystals from
 434 lapilli and pumices (Pavin's Group of Volcanoes) and mantle enclaves (Puy Beaunit). (a) Primary negatively-shaped
 435 fluid inclusions (*FI*) in an olivine crystal from Montcineyre. (b) Secondary rounded fluid inclusions (*F3*) in an olivine
 436 crystal from Montcineyre. (c) Secondary rounded fluid inclusions (*F5*) from an olivine crystal from Montcineyre that
 437 present a heterogeneous trapping with both single-phase fluid inclusions (*c1*) and a mixture of liquid-vapor phases (*c2*).
 438 (d) Secondary negatively-shaped fluid inclusions (*fi*) in a clinopyroxene crystal from the Iherzolite. (e) Continuous trail
 439 of secondary fluid inclusions cutting both olivine and clinopyroxene crystals from the harzburgite. Note the inclusions
 440 of olivine in the clinopyroxene crystal. Fluid inclusions have a necking down shape in the olivine crystal (*e1*) but are
 441 rounded in the clinopyroxene crystal (*e2*). (f) Trail of secondary fluid inclusions in a clinopyroxene crystal from the
 442 harzburgite that stops at the contact with the olivine crystal.
 443



444
 445
 446
 447
 448
 449
 450
 451

Fig. 5. Distribution of CO₂ density in fluid inclusions from olivine, clinopyroxene, and orthopyroxene from mantle enclaves (Puy Beauunit) and lapilli and pumices (Pavin's Group of Volcanoes). FIs: Fluid Inclusions. "With secondary phases" denotes the crystals where either sulphate-sulphide-SO₂ or carbonate were detected in fluid inclusions by Raman spectroscopy. (a) and (b) show the effect of the presence of either sulphate-sulphide or SO₂ in fluid inclusions on the distribution of CO₂ densities. (c) and (d) show the effect of the presence of carbonates in fluid inclusions on the distribution of CO₂ densities.



452
 453 **Fig. 6.** 2D section of some fluid inclusions extracted from the 3D Raman images. (a) FI1, FI2, FI3 are three single fluid
 454 inclusions from a trail of secondary fluid inclusions in an olivine crystal from Montcineyre. (b) Fla is one fluid
 455 inclusion in a trail of secondary fluid inclusions cutting a clinopyroxene crystal of the harzburgite. The size of the
 456 inclusions and the raw CO₂ density (i.e., not calculated by considering the presence of a CO₂-H₂O initial mixture) of the
 457 gas phase are reported.

458
 459 **4.3. Noble gases and carbon isotopes of CO₂**

460 Noble gas abundances and isotopic composition, together with CO₂ abundance and carbon isotopy
 461 ($\delta^{13}\text{C}$) of CO₂ obtained by crystal crushing are given in **Table 3**. The helium abundance (⁴He)
 462 varies from 4.6×10^{-13} mol/g (harzburgite) to 3.5×10^{-12} mol/g (Iherzolite) with the highest
 463 abundances in orthopyroxene crystals and the lowest ones in olivine crystals. Crystal crushing from
 464 the tephras of the Pavin's Group of Volcanoes yields a more restricted range of abundances ($1.2 -$
 465 2.0×10^{-12} mol/g). ⁴He/²⁰Ne measured in our samples varies from 60 to 5603. Rc/Ra values vary
 466 from 6.5 to 6.8 for crystals from tephras, with an increase from Pavin to Montchal to Montcineyre
 467 products (**Fig. 7a**). This variability is close to the analytical uncertainty ($2\sigma = 0.2$ for tephras) and
 468 requires to be cautious about this potential increase between products. Rc/Ra values vary from 6.6
 469 to 7.0 for crystals from mantle enclaves, with higher values in orthopyroxene crystals than in
 470 olivine ones (**Fig. 7a**). The range of ⁴He abundances and Rc/Ra values measured in our study is
 471 consistent with previous measurements obtained in mantle enclaves from the CEVP (Buikin et al.,
 472 2005; Gautheron et al., 2005; Rizzo et al., 2018, 2021).

473 The ⁴⁰Ar/³⁶Ar varies from 325 to 2735, which is higher than the atmospheric signature
 474 (⁴⁰Ar/³⁶Ar = 298.56; Lee et al., 2006). ⁴He/⁴⁰Ar* ranges from 4.0 to 16.2 for crystals from tephras
 475 with an increase from Montcineyre to Montchal to Pavin products (**Fig. 7b**). ⁴He/⁴⁰Ar* varies from

476 0.3 to 1.5 for crystals from mantle enclaves, with the lowest values for the Iherzolite (0.3 and 0.7 for
477 orthopyroxene and olivine crystals, respectively). The systematic increase of $^4\text{He}/^{40}\text{Ar}^*$ from
478 orthopyroxene crystals to olivine crystals coupled with a decrease of ^4He abundances (and of
479 Rc/Ra) discards any diffusive fractionation of noble gases between orthopyroxene and olivine
480 crystals (**Fig. 7b**) (Yamamoto et al., 2009; Rizzo et al., 2018, 2021).

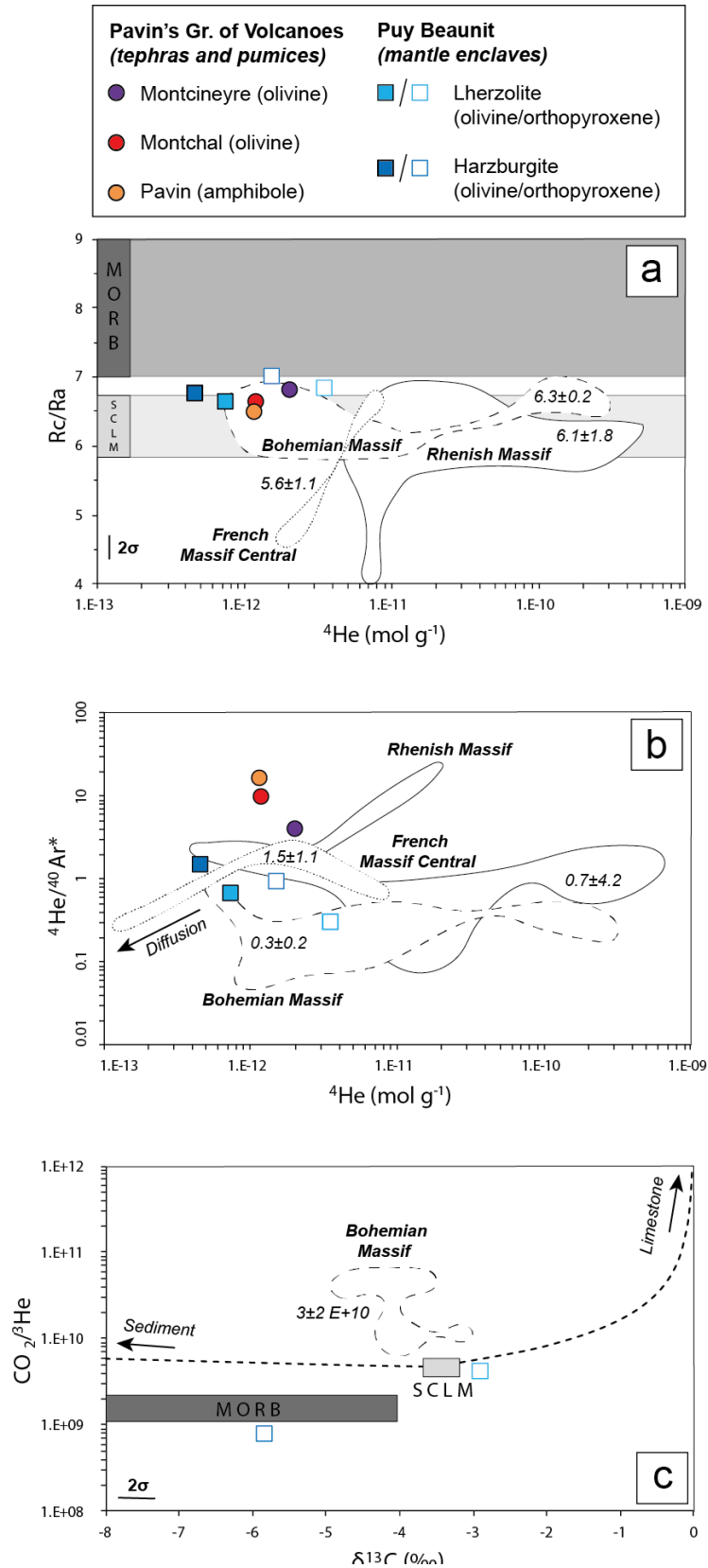
481 The $\text{CO}_2/{}^3\text{He}$ ratio ranges from 1.6×10^8 to 4.0×10^9 for mantle enclaves at Puy Beaunit,
482 with the lowest value measured in olivine crystals and the highest value measured in orthopyroxene
483 crystals from the Iherzolite. The range of values for tephras from the Pavin's Group of Volcanoes is
484 narrower ($1.1 - 3.1 \times 10^8$). The analysis of carbon isotopes of CO_2 was possible only by crushing
485 orthopyroxene crystals from both Iherzolite and harzburgite due to their higher gas abundance
486 (**Table 3**). $\delta^{13}\text{C}$ of CO_2 varies from -2.9 ‰ for the Iherzolite (close to the range of documented
487 values for mantle enclaves within the CEVP) down to -5.8 ‰ for the harzburgite (**Fig. 7c**).

488
489 Measurements of dissolved gases in Lake Pavin (at 70 and 90 m-depth) in 2021 yielded Rc/Ra
490 values in the range 6.5-6.7, and $\delta^{13}\text{C}$ of CO_2 varying from -2.8 to 0.8 ‰ (**Table 4**). Gas emissions
491 from the Escarot mofettes sampled in 2021 show slightly lower Rc/Ra (= 6.1) and $\delta^{13}\text{C}$ of CO_2 (= -
492 3.4 ‰) than those reported for the Pavin Lake (**Table 4**). The $^4\text{He}/^{40}\text{Ar}^*$ and the $\text{CO}_2/{}^3\text{He}$ are equal
493 to 1.7 and 5.3×10^9 , respectively.

494

495

496



497
498
499
500
501
502
503
504
505

Fig. 7. (a) ${}^4\text{He}$ abundance vs. Rc/Ra , (b) ${}^4\text{He}$ abundance vs. ${}^4\text{He}/{}^{40}\text{Ar}^*$, and (c) $\delta^{13}\text{C}$ vs. $\text{CO}_2/{}^3\text{He}$ from the gas entrapped in fluid inclusions and released by crystal crushing. The distribution fields of the literature data for the CEVP (French Massif Central, Bohemian Massif, Rhenish Massif) are reported as well as the average value for each field. Data sources: Buikin et al. (2005), Gautheron and Moreira (2002), and Rizzo et al. (2018). SCLM, MORB, Limestone and Sediment endmembers from Sano and Marty (1995), Gautheron and Moreira (2002), Bräuer et al. (2016, 2017), and Rizzo et al. (2018).

506

507

508 **5. Discussion**

509 **5.1. Architecture of the magmatic system beneath the Pavin's Group of Volcanoes**

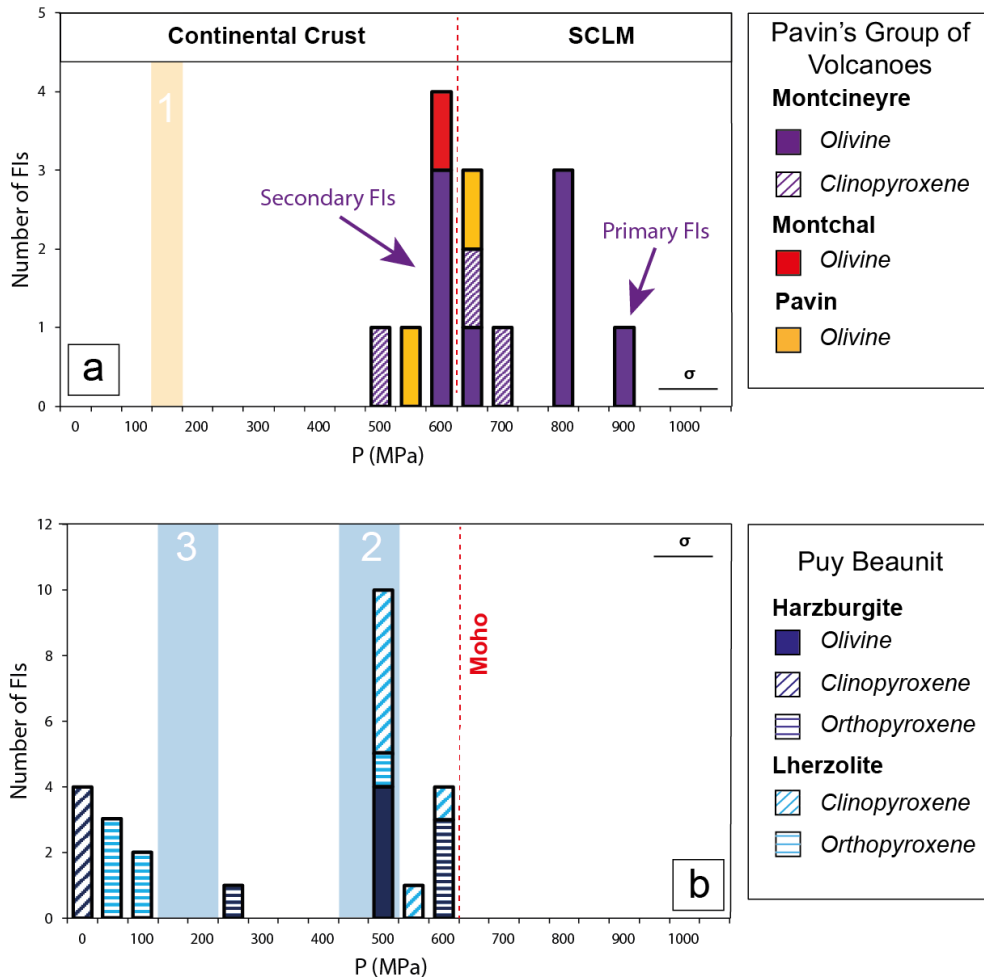
510 Barometry based on CO₂ density in fluid inclusions is extensively used to decipher the architecture
511 of magmatic systems by pointing out the pressure of magma crystallisation and ponding zones
512 during magma ascent (see Hansteen and Klügel (2008) for a complete review). To reach this aim, a
513 careful analysis of the post-entrapment processes that may affect fluid inclusions is required to
514 avoid erroneous interpretation (cf. "Roedder's rules"; Roedder, 1984). The fluid inclusions FI1-FI2-
515 FI3 described in a trail of secondary fluid inclusions in an olivine crystal from Montcineyre (**Fig.**
516 **6a**) are a representative example of a process of CO₂ density decrease due to either post-entrapment
517 volumetric re-equilibration (stretching or decrepitation) or carbonate precipitation (Schiavi et al.,
518 2020; Venugopal et al., 2020). If we assume that the CO₂ density and the volume of FI1-FI2 were
519 identical to those of FI3 at the moment of the entrapment, then the amount of CO₂ in fluid
520 inclusions should remain the same in time, independently of the volumetric change. By considering
521 the volume of FI1-FI2-FI3 and the measured CO₂ density, the amount of CO₂ in fluid inclusions
522 varies by more than an order of magnitude (from 2.2×10^{-11} g of CO₂ in FI3 to $5.9-6.6 \times 10^{-10}$ g
523 of CO₂ in FI1) (**Table 5**). Accordingly, a scenario of post-entrapment volumetric re-equilibration
524 starting with three inclusions of the same size and density cannot explain the variability of CO₂
525 density in this trail of secondary fluid inclusions. We recognise that the actual importance of post-
526 entrapment volumetric re-equilibration cannot be quantified precisely because the initial size of the
527 inclusions is not known. However, one can anticipate that this process plays a minor role in
528 explaining the variability of CO₂ density compared to that of carbonate precipitation in our study.
529 Indeed, by using 3D Raman imaging to estimate the amount of CO₂ consumed to form carbonates
530 in FI1 and FI2 (see Methods; Schiavi et al., 2020) we obtain a similar initial CO₂ density for the two
531 inclusions: 1.06 ± 0.09 and 1.12 ± 0.07 g/cm³, respectively (instead of a measured CO₂ density of 0.88
532 and 0.92 g/cm³, respectively) (**Table 5**). Considering the total uncertainty, $\epsilon(\text{TOT})$, on
533 measurements of CO₂ density in fluid inclusions in our study (0.05 g/cm³; see Methods), these
534 values overlap with the CO₂ density measured in FI3 (1.0 g/cm³) where carbonate was not detected
535 on Raman spectra. A similar calculation was performed in a fluid inclusion (FIa) hosted in a trail of
536 secondary fluid inclusions cutting a clinopyroxene crystal of the harzburgite and where carbonate
537 was detected on Raman spectra (**Fig. 6b**). The CO₂ density increases from 0.14 g/cm³ (measured) to
538 0.26 ± 0.09 g/cm³ (**Table 5**). These calculations show that carbonate formation in fluid inclusions
539 may lead to an underestimation of CO₂ density in fluid inclusions by up to 50 % and thus to
540 unreliable barometric estimates. To limit this effect, in the following parts, we filtered our dataset
541 by considering only fluid inclusions free of solid phases and of small diameter (<4 μm) (**Fig. 8**).
542 The selection of small inclusions is justified because, within the same family of fluid inclusions,
543 secondary solid phases are more abundant and/or CO₂ density is lower in larger fluid inclusions.
544 Such a protocol is in line with previous recommendations made to discard fluid inclusions affected
545 by post-entrapment processes (Wanamaker and Evans, 1989; Frezzotti and Touret, 2014; Boudoire
546 et al., 2018).

547

548 Beneath the Chaîne des Puys (close to the area of study; **Fig. 1**), the Moho was imaged at a depth of
549 24 km, which corresponds to a pressure of about 650 MPa considering an average crustal density of
550 2750 kg.m^{-3} for the European plate (Spooner et al., 2019). Fixing the temperature at 1300 °C for
551 Montcineyre, 1200 °C for Montchal, and 1050 °C for Pavin (see section 3.4), barometric estimates
552 from the fluid inclusions in crystals from lapilli and pumices of the Pavin's Group of Volcanoes
553 define two main modes (**Fig. 8a**): (1) at 800-900 MPa and at (2) 600-700 MPa. The first mode is
554 only observed in olivine-hosted fluid inclusions from Montcineyre. A maximum pressure of 903
555 MPa is recorded in primary fluid inclusions that may represent a deep magma crystallisation zone
556 (of olivine) in the lithospheric mantle. Actually, Montcineyre olivine phenocrysts have the highest

557 average forsterite content (Fo_{83-84}) among the olivine crystals of the Pavin's group of volcanoes.
558 This is consistent with the primitive nature of basanitic lavas erupted at Montcineyre (Villemant et
559 al., 2016), but also shows that advanced differentiation processes already occurred in the
560 lithospheric mantle as the forsterite content in our samples does not exceed $Fo_{85.8}$. The second mode
561 of barometric estimates corresponds to the Moho depth and is defined by most of the secondary
562 fluid inclusions hosted in olivine and clinopyroxene crystals from Montcineyre, Montchal and
563 Pavin. As documented beneath many volcanic provinces (Jennings et al., 2017; Boudoire et al.,
564 2021), the boundary zone between the lithospheric mantle and the crust could be a major interface
565 beneath the area for (1) magma ponding, as indicated by partial or total re-equilibration of some
566 primary fluid inclusions and by the similarity of CO_2 density in distinct families of fluid inclusions
567 (**Table 2**), (2) magma mixing, as suggested by the complex normal and reverse zoning patterns
568 observed in both olivine and clinopyroxene crystals, and by their large range of compositions
569 (**Table 1**), and (3) advanced magma differentiation involving olivine and clinopyroxene fractional
570 crystallisation (**Fig. 3**). The barometric estimates obtained in our study from Pavin's pumice (596-
571 663 MPa, i.e., Moho depth) differ from pre-eruptive barometric conditions set by experimental
572 petrology (150-200 MPa, i.e., crustal level; Rondet et al., 2019) (**Fig. 8a**). This discrepancy is
573 presumably due to the fact that our barometric estimations are based on fluid inclusions in olivine
574 crystals. Such olivine crystals are rare in Pavin's pumice, in which plagioclase, amphibole and
575 clinopyroxene are the most abundant crystals, and unusual for differentiated benmoreitic magmas
576 (Rondet et al., 2019). They may be either xenocrysts from older surrounding volcanic rock material
577 carried during the explosive eruption (Villemant et al., 2016) or phenocrysts from a more primitive
578 melt that mixed with the benmoreitic magma at crustal level before the eruption. Further work is
579 required to evaluate these hypotheses.

580 Considering a temperature of 850 °C for the lherzolite and 1000 °C for the harzburgite (see
581 section 3.4), barometric estimates from the fluid inclusions in crystals from mantle enclaves of Puy
582 Beaunit range from 26 to 636 MPa for the harzburgite and from 96 to 624 MPa for the lherzolite
583 with a main mode around 500-550 MPa (**Fig. 8b**). These pressures are essentially crustal and are far
584 from what one may expect for mantle enclaves. Despite the filtering of the fluid inclusions
585 described above, it is clear that the inclusions have undergone post-entrapment re-equilibration
586 processes such as stretching or decrepitation. Interestingly, we note that helium abundances released
587 by crystal crushing from mantle enclaves are quite similar (if not lower) to those from tephros
588 (**Table 3**). This result contrasts with what we observed, for example, at the Piton de la Fournaise
589 volcano, Réunion Island (Boudoire et al., 2018), where the total gas content released by crystal
590 crushing increases with pressure. The extensive post-entrapment re-equilibration observed at Puy
591 Beaunit better supports the idea of a partial decrepitation of fluid inclusions during the ascent of the
592 magma carrying the mantle enclaves. The main mode of barometric estimates around 500-550 MPa
593 corresponds to the deepest pressure mode measured in fluid inclusions in phenocrysts from lavas at
594 Puy Beaunit (**Fig. 8b**; Bilal and Touret, 1977). This good pressure match suggests magma ponding
595 at this depth (Bilal and Touret, 1977), in which the pressures in the fluid inclusions from mantle
596 enclaves have been reset.
597



598
599

600 **Fig. 8.** Distribution of barometric estimates calculated from filtered CO₂ density in fluid inclusions (see Methods) in
601 crystals from (a) tephros of the Pavin's Group of Volcanoes and (b) mantle enclaves at Puy Beaunit. Shaded bar 1
602 highlights the pre-eruptive barometric conditions for the Pavin explosive event (Rondet et al., 2019). Shaded bars 2 and
603 3 are the two barometric modes identified from fluid inclusions in phenocrysts from lavas at Puy Beaunit (Bilal and
604 Touret, 1977).
605

606 5.2. Origin and evolution of the magmatic fluids

607 The Sub-Continental Lithospheric Mantle beneath the FMC was extensively studied by
608 petrological, geochemical, and geophysical means (Lenoir et al., 2000; Féménias et al., 2001, 2004;
609 Babuška et al., 2002; Uenver-Thiele et al., 2014, 2017). Compared to the southern domain, the
610 northern lithospheric domain of the FMC, where our sampling sites are located, is more refractory
611 and oxidised due to several episodes of melt extraction and metasomatism by subduction-related
612 fluids during Variscan times, including local carbonatite metasomatism (Uenver-Thiele et al.,
613 2017). These phenomena are documented in detail in mantle enclaves at Puy Beaunit (Féménias et
614 al., 2004).

615 In our study, the increase in MgO in olivine, clinopyroxene, and orthopyroxene (**Fig. 3a**)
616 together with the decrease in Al₂O₃ in clinopyroxene and orthopyroxene (**Fig. 3b, c**) from
617 granuloblastic lherzolite to transitional harzburgite are similar to previous observations made
618 beneath the Rhenish Massif, for instance (see Rizzo et al., 2021, for a review). These trends
619 highlight the transition from a fertile mantle source (lherzolite) towards a more refractory mantle
620 source (harzburgite) (Arai, 1994; Bonadiman et al., 2011; Upton et al., 2011).

621 We showed that ⁴He/⁴⁰Ar* and Rc/Ra values increase while CO₂/³He and δ¹³C decrease
622 from the lherzolite to the harzburgite (**Fig. 7**). These trends contrast with the decrease in ⁴He/⁴⁰Ar*
623 and Rc/Ra classically associated to partial melting (Yamamoto et al., 2009) and rather suggest
624 preferential metasomatic enrichment of the refractory mantle subsequent to partial melting and melt

625 extraction. The slight increase in CaO and MgO in olivine crystal rims as well as the decrease in
626 Al₂O₃ coupled with the increase in MgO in orthopyroxene crystal rims (**Fig. 3a, c**) may testify of
627 this interaction with a metasomatic agent. Higher Rc/Ra values together with lower CO₂³He and
628 δ¹³C for harzburgite are consistent with an enrichment due to fluids with MORB-like features (**Fig.**
629 **7a, c**). Similar enrichment processes of the SCLM were documented beneath the Bohemian Massif
630 (Matusiak-Malek et al., 2017; Rizzo et al., 2018), the Rhenish Massif (Rizzo et al., 2021), and the
631 FMC (Uenver-Thiele et al., 2017).

632 In both harzburgite and lherzolite, we also documented higher Rc/Ra and lower ⁴He/⁴⁰Ar*
633 values in orthopyroxene with respect to olivine (**Fig. 7a, b**). This observation is common in mantle
634 enclaves from the CEVP (Rizzo et al., 2018) and suggests partial recrystallisation of orthopyroxene.
635 Actually, we noted that (1) trails of secondary fluid inclusions preferentially cut orthopyroxene
636 rather than olivine crystals (**Fig. 4e, f**) and (2) gas abundance released by crystal crushing is higher
637 for orthopyroxene. These observations support the idea of preferential recrystallisation and fluid
638 inclusions entrapment in orthopyroxene under the influence of a metasomatic agent.
639

640 Noble gases in fluid inclusions in crystals from tephros of the Pavin's Group of Volcanoes exhibit a
641 range of Rc/Ra values (6.5-6.8) similar to the range in mantle enclaves at Puy Beaunit (6.6-7.0).
642 These first values obtained from phenocrysts in lavas suggest that the magma erupted at the Pavin's
643 Group of Volcanoes could be directly linked to partial melts from the local SCLM (Rc/Ra from 5.2
644 to 7.0; Gautheron and Moreira, 2002). The main difference in noble gases between tephros and
645 mantle enclaves concerns ⁴He/⁴⁰Ar* (**Fig. 7b**). Higher values for tephros (>4) are not reconcilable
646 with either (1) an effect of various partial melting degrees of the mantle source (Yamamoto et al.,
647 2009), whose ⁴He/⁴⁰Ar* values are systematically lower than 1.5, or (2) a process of diffusive
648 fractionation (Trull and Kurz, 1993) that should decrease both ⁴He/⁴⁰Ar* and Rc/Ra.

649 Conversely, in magmatic rocks, an increase of the ⁴He/⁴⁰Ar* can be indicative of a process
650 of magma degassing due to the higher solubility of He in silicate melts with respect to Ar (Burnard,
651 2004). With the aim of testing this hypothesis, we modelled degassing trends using the equations of
652 Batch Equilibrium Degassing (BED) and of Fractional Equilibrium Degassing (FED) for ⁴He/⁴⁰Ar*,
653 ⁴He/CO₂ and δ¹³C (Jambon et al., 1986; Shaw et al., 2004). The complete description of the
654 equations is detailed in Boudoire et al. (2018). Starting conditions were defined as follows:

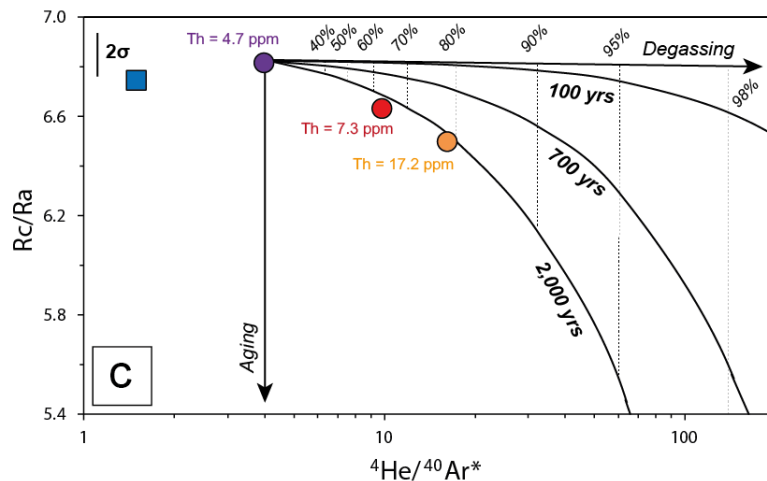
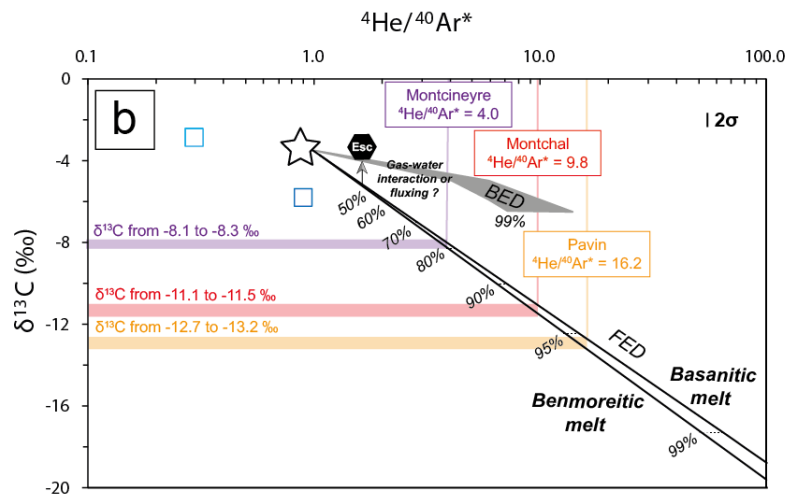
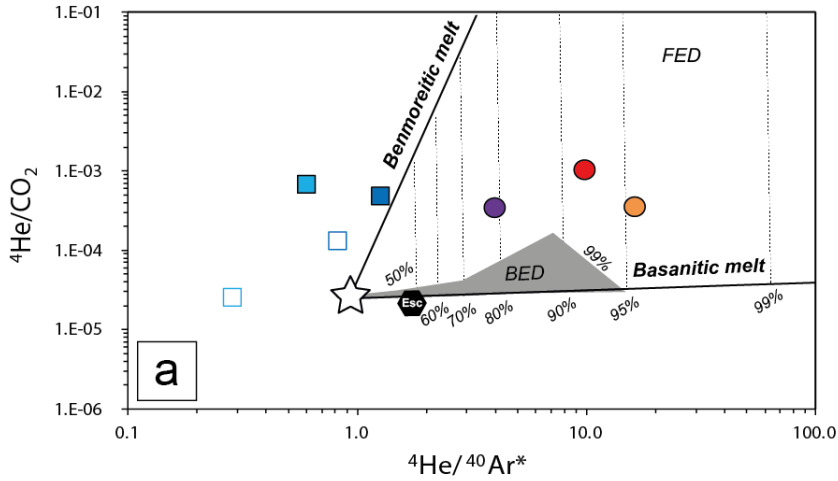
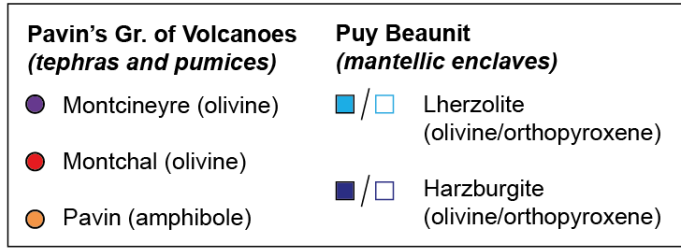
- 655 (1) Initial ratios correspond to the values already defined for the SCLM associated to the
656 ECRS (Bräuer et al., 2017; Rizzo et al., 2018). ⁴He/⁴⁰Ar* was fixed at 1.0. This value is
657 similar to the values measured (i) in fluid inclusions in the orthopyroxene crystals of the
658 harzburgite analysed in this study (⁴He/⁴⁰Ar* = 0.9) and (ii) in fluid inclusions in crystals
659 from phlogopite/amphibole-bearing mantle xenoliths along the ECRS (Rizzo et al.,
660 2021). This choice is further supported by the fact that low-silica magmas such as
661 basanites (Montcineyre) cannot be produced by partial melting of dry lherzolite in the
662 SCLM but rather require the presence of metasomatic lithologies (Pilet, 2015) as
663 suggested for the harzburgite in our study. ⁴He/CO₂ was set at 2.5 × 10⁻⁵ and δ¹³C at -
664 3.5 ‰. These values are similar to the values proposed by Rizzo et al. (2018). They are
665 also in the range of those defined for the SCLM in Europe (δ¹³C from -3.5 to -2 ‰) by
666 Bräuer et al. (2017) and close to the values obtained in fluid inclusions in orthopyroxene
667 crystals from the lherzolite analysed in this study (**Fig. 7c**).
- 668 (2) Solubilities of He, Ar and CO₂ (S_{He}, S_{Ar}, S_{CO2}) were estimated for basanitic and
669 benmoreitic melts to cover the magmatic variability of the Pavin's Group of Volcanoes.
670 We used the model of Iacono-Marziano et al. (2010) for He and Ar, and that of Eguchi
671 and Dasgupta (2018) for CO₂ (**Appendix 3**). These models require an estimation of the
672 composition and density of the magma, and of the pressure-temperature conditions.
673 Importantly, S_{He}/S_{Ar} remains quite constant, whereas S_{He}/S_{CO2} increases during magma
674 ascent (Boudoire et al., 2018). Note that the solubility of CO₂ depends significantly on
675 melt composition, especially for alkaline melts (Iacono-Marziano et al., 2010; Eguchi

- 676 and Dasgupta, 2018). As a result, the degassing curves show a higher variability of
677 $^4\text{He}/\text{CO}_2$ (relative to $^4\text{He}/^{40}\text{Ar}^*$) depending on melt composition.
- 678 (3) The carbon isotope fractionation factor between vapour and melt (Δ) was fixed at 3 ‰ in
679 accordance with the average value of experimental and natural data (Javoy et al., 1978;
680 Aubaud et al., 2005; Paonita et al., 2012).
- 681 (4) The composition of the lava erupted at Montcineyre (sample P13-8; Villemant et al.,
682 2016) and at Pavin (sample KBP3b*; Villemant et al., 2016) was taken as representative
683 of the basanitic and benmoreitic melts, respectively (**Appendix 3**). The density of the
684 melts was calculated from the equation of Lange and Carmichael (1990).
- 685 (5) Temperature was calculated from the composition of the lava by using the equation of
686 Putirka (2008): 1300 °C at Montcineyre and 1050 °C at Pavin. Pressure was fixed at 650
687 MPa (Moho depth) in accordance with most of the barometric estimates obtained in this
688 study for the products of the Pavin's Group of Volcanoes (**Appendix 3**).

689 The modelling of magma degassing revealed that the $^4\text{He}/^{40}\text{Ar}^*$ variability is best explained by a
690 FED process (**Fig. 9a**). The degree of magma degassing increases from Montcineyre (basanite) to
691 Montchal (hawaiite) to Pavin (benmoreite), and thus mirrors the differentiation trend of the Pavin's
692 Group of Volcanoes. We note that even the more primitive melt at Montcineyre, with barometric
693 estimates referring to mantle level, is already strongly degassed ($\approx 80\%$) with respect to primary
694 mantle conditions. This indicates that melts stored in the lithospheric mantle beneath the area have
695 already undergone an advanced degree of degassing and differentiation (in agreement with the
696 absence of olivine crystals with forsterite content exceeding $\text{Fo}_{85.8}$, as discussed above). A similar
697 conclusion was reached in other volcanic systems, such as in oceanic islands at Piton de la
698 Fournaise (La Réunion; Boudoire et al., 2018) or El Hierro (Canary Islands; Longpré et al., 2017),
699 and attributed to early magmatic processes occurring in deeper mantle storage zones. Such an
700 advanced degree of degassing is expected to have an important impact on $\delta^{13}\text{C}$ values of the vapour
701 phase exsolved from melts of the Pavin's Group of Volcanoes due to preferential partitioning of ^{13}C
702 in gas bubbles (Aubaud et al., 2004). Unfortunately, direct measurements of $\delta^{13}\text{C}$ of CO_2 released
703 by crystal crushing was analytically impossible in these samples due to a low gas abundance. By
704 using the same starting conditions as reported above, we can calculate the expected $\delta^{13}\text{C}$ of CO_2 in
705 the vapour phase (**Fig. 9b**): from -8.1/-8.3 ‰ at Montcineyre down to -12.7/-13.2 ‰ at Pavin (for a
706 melt composition that spans between basanite and benmoreite). These estimations show that very
707 negative $\delta^{13}\text{C}$ values may be reached with a "purely" magmatic contribution without (1) mixing
708 with ^{13}C -depleted compounds (organic matter, C3-C4 plants; Boudoire et al., 2022) or (2) a CO_2
709 condensation process (Mook et al., 1974).

710 A potential slight decrease of Rc/Ra with time in the fluid inclusions of the Pavin's Group of
711 Volcanoes may be observed (**Fig. 9c**). If established (the variability is almost overlapped by the
712 analytical uncertainty), this decrease is not reconcilable with degassing processes, as this ratio does
713 not fractionate. More likely, it could result from progressive enrichment in ^4He due to (1) magma
714 degassing coupled to aging and/or (2) crustal contamination (Kurz et al., 1996; Moreira, 2013) (**Fig.**
715 **9c**). We recognise that further work is required to investigate the role of these processes in the
716 magma evolution of the Pavin's Group of Volcanoes.

717



719

720

721

722

723

724

725

726

727

728

729

730

731

732

733

734

735

736

737

738

739

740

741

742

743

744

745

746

747

748

749

750

751

752

753

754

755

756

757

758

759

760

761

762

763

764

765

766

767

768

769

770

771

Fig. 9. (a) Modelling of the evolution of ${}^4\text{He}/{}^{40}\text{Ar}^*$ and ${}^4\text{He}/\text{CO}_2$ during degassing. (b) Modelling of the evolution of $\delta^{13}\text{C}$ of CO_2 by degassing. The values of $\delta^{13}\text{C}$ of CO_2 for the vapour phase exsolved from the melts of the Pavin's Group of Volcanoes are estimated by coupling the measured ${}^4\text{He}/{}^{40}\text{Ar}^*$ and the theoretical curves of fractional equilibrium degassing for basanitic and benmoreitic melts. (c) Modelling of the aging-degassing processes in the Pavin's Group of Volcanoes: evolution of Rc/Ra and ${}^4\text{He}/{}^{40}\text{Ar}^*$ in the vapour phase exsolved from the melts. Th is the composition in thorium of the lavas (Villemant et al., 2016). The amount of radiogenic ${}^4\text{He}$ ingrowth (in cm^3/g) from the decay of U and Th over time (${}^4\text{He}^*$) in magma can be estimated through the equation of Graham et al. (1987): ${}^4\text{He}^* = 2.8 \times 10^{-8} \times [\text{U}] \times (4.35 + \frac{\text{Th}}{\text{U}}) \times t$ where t is the time in Ma, [U] is the uranium concentration in ppm (1.3 ppm in sample P13-8 at Montcineyre; Villemant et al., 2016), and Th/U is the thorium-uranium atomic ratio (3.6 for the same sample). FED: Fractional Equilibrium Degassing, BED: Batch Equilibrium Degassing (grey field for the full field of values considering either a basanitic or a benmoreitic composition). The white star represents the starting conditions in the SCLM (see text for explanations). The black polygon highlights the chemical composition of the gas emissions at the Escarot mofettes.

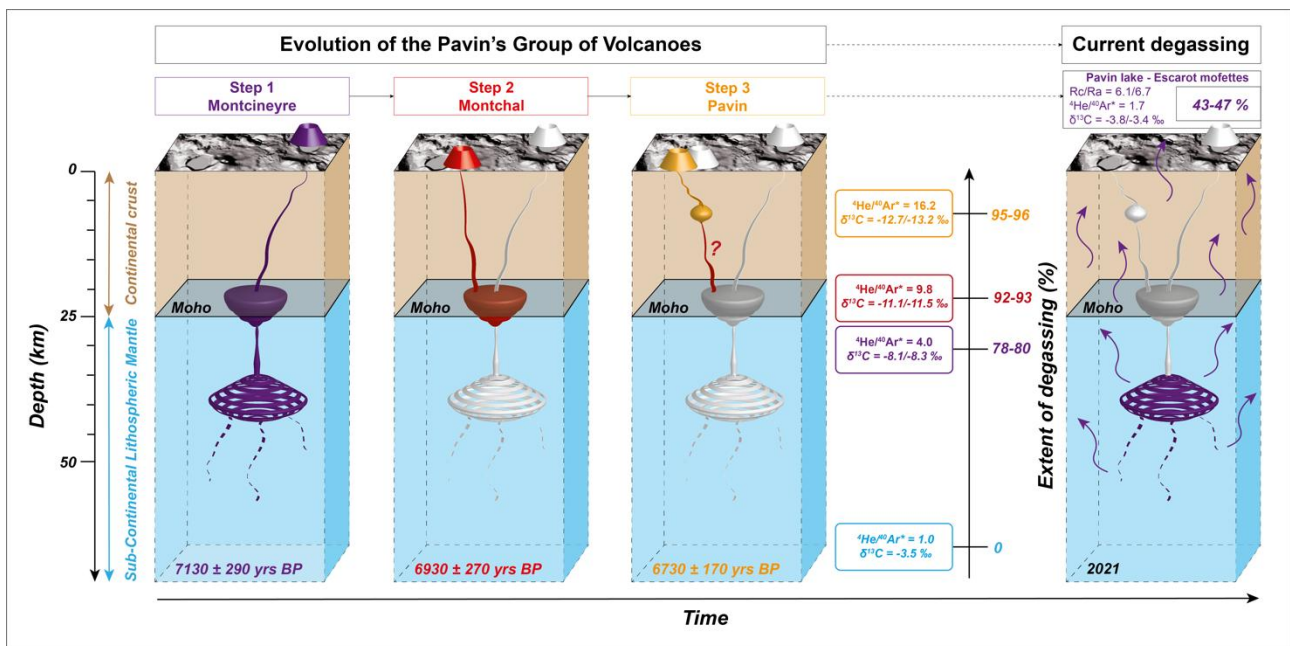
5.3. Implications for the monitoring of a long-quiet volcanic province

By coupling barometric estimates and the extents of degassing based on ${}^4\text{He}/{}^{40}\text{Ar}^*$ (starting from an initial ratio of 1.0 at the source; see previous section) we can build an interpretative scheme of the magma plumbing system beneath the Lake Pavin area and of the evolution of the exsolved gas phase (**Fig. 10**). The magma differentiation documented for the Pavin's Group of Volcanoes (Villemant et al., 2016; Rondet et al., 2019) is accompanied by progressive magma degassing together with a decrease of the pressure of magma ponding from Montcineyre (basanite, ${}^4\text{He}/{}^{40}\text{Ar}^* = 4.0$, Moho depth and deeper) to Montchal (hawaiiite, ${}^4\text{He}/{}^{40}\text{Ar}^* = 9.8$, Moho depth) to Pavin (benmoreite, ${}^4\text{He}/{}^{40}\text{Ar}^* = 16.2$, crustal level).

The model in Figure 10 sheds new light on the origin of current gas emissions in the area. Previous measurements of dissolved gases in Lake Pavin between 1969 and 1996 show an Rc/Ra value of 6.5 below the chemocline at 60 m-depth (Aeschbach-Hertig et al., 1999; Olive and Boulègue, 2004). Our measurements in 2021 yield a Rc/Ra in the range 6.5-6.7 (**Table 4**) that is consistent with previous analyses. In gas emissions from the Escarot mofettes, a Rc/Ra in the range of 6.0-6.3 and a $\delta^{13}\text{C}$ from -3.8 to -3.6 ‰ were documented in 2011-2015 (Bräuer et al., 2017). The measurements we performed in 2021 (Rc/Ra = 6.1 and $\delta^{13}\text{C} = -3.4$ ‰; **Table 4**) are similar to these values. In addition to the stability of these geochemical markers in time, it is worth noting the high Rc/Ra values in the surface gas emissions, which are the most elevated in the FMC until now (Bräuer et al., 2017). These high Rc/Ra values are close to those documented in the gas entrapped in fluid inclusions from mantle enclaves at Puy Beaunit (Rc/Ra = 6.6-7.0) and from tephras belonging to the Pavin's Group of Volcanoes (Rc/Ra = 6.5-6.8). In addition, ${}^4\text{He}/{}^{40}\text{Ar}^*$ was measured at 1.7 in the gas emissions from the Escarot mofettes (**Table 4**). According to our degassing model and interpretative scheme, such a value should place the depth of degassing at mantle level (**Fig. 10**). This suggests the absence of a residual crustal magma reservoir involved in feeding the surface gas emissions in the Lake Pavin area and rather supports the idea of fluid transport along deep reaching faults from a magma reservoir within the SCLM (Bräuer et al., 2017). However, in the event of a new batch of magma rising from mantle depth to shallower levels, our interpretative scheme allows us to predict a slight increase in Rc/Ra (less crustal contamination and/or less ageing) and in ${}^4\text{He}/{}^{40}\text{Ar}^*$ (by degassing upon magma ascent) with respect to current values measured in local gaseous emissions. Considering this scenario, we recommend that an appropriate monitoring strategy for gaseous emissions in the area be put in place. In particular, we highlight the necessity to sustain a long-term monitoring of noble gases in several mineral springs representative of the chemical heterogeneity of these markers on a regional scale (Bräuer et al., 2017).

In our model, if ${}^4\text{He}/{}^{40}\text{Ar}^*$ increases by degassing in gas emissions from the Escarot mofettes up to 1.7 (with respect to the starting conditions in the SCLM), $\delta^{13}\text{C}$ of CO_2 is expected to decrease down to -5.2/-5.4 ‰ in gas emissions from the Escarot mofettes. Such a discrepancy with the measured value (-3.4 ‰; **Table 4**) is intriguing. A first hypothesis to reconcile these values is to consider a process of partial dissolution of CO_2 in shallow aquifers. Under appropriate pH and

772 temperature conditions such a process may trigger the Rayleigh fractionation of CO₂ towards more
 773 positive values of δ¹³C (Mook et al., 1974; Hoefs, 1997). It could also partially explain the
 774 enrichment in He and CH₄ (Caracausi et al., 2003) with respect to the composition of other local gas
 775 emissions (Bräuer et al., 2017). A second hypothesis to explain the relatively high value of δ¹³C of
 776 CO₂ measured at the Escarot mofettes is to consider a process of CO₂ fluxing from depth. Indeed,
 777 the extensive CO₂ degassing we documented in this study (more than 80 % of the initial CO₂ would
 778 be lost for melts of the Pavin's Group of Volcanoes) suggests the presence of a deeper CO₂ vapour
 779 phase. This inference is supported by recent results in experimental petrology that show a
 780 significant enrichment in volatile elements in primary mantle melts beneath the FMC (Buso et al.,
 781 2022). This CO₂ phase, exsolved early and thus characterised by a less negative δ¹³C of CO₂, may
 782 contribute to flux overlying magma reservoirs (Edmonds, 2008) and consequently to modify the
 783 pristine signature of the melt-related CO₂. Carbon dioxide fluxing may also affect the solubility of
 784 other gaseous species like H₂O and SO₂, and thus potentially lead to the early exsolution of an
 785 enriched H₂O-S vapour phase (Spilliaert et al., 2006; Boudoire et al., 2021). This process may
 786 provide an explanation to the detection of SO₂ and/or sulphate-sulphide by Raman spectroscopy in
 787 some fluid inclusions entrapped at mantle level (Fig. 5) whereas SO₂ is expected to strongly degas
 788 only at crustal levels (<250 MPa; Boulling and Wood, 2022). Further work is required to evaluate
 789 these hypotheses but in light of them it seems relevant to pursue the monitoring of gas emissions
 790 from the Escarot mofettes and to promote the installation of a soil CO₂ station there.
 791



792
 793
 794 **Fig. 10.** Interpretative scheme of the evolution in time of the magmatic system and of the composition of the exsolved
 795 vapor phase for the Pavin's Group of Volcanoes obtained by coupling (1) barometric estimates, (2) measured ⁴He/⁴⁰Ar*,
 796 (3) estimated δ¹³C of CO₂ from fluid inclusions. A comparison is made with the current status of degassing in the area
 797 (composition of dissolved gases in Lake Pavin and of gas emissions from the Escarot mofettes). The question mark in
 798 step 3 denotes the hypothesis of a potential pre-eruptive arrival of deep magmatic fluids in the crustal magma reservoir
 799 of the Pavin eruption (150-200 MPa; Rondet et al., 2019). Equivalent depth was calculated considering the Moho depth
 800 at 24 km and average crustal and mantle densities for the European plate of 2750 and 3300 kg.m⁻³, respectively
 801 (Spooner et al., 2019).
 802

803 6. Conclusion

804 We conducted a coupled study of CO₂ densimetry and geochemistry of fluid inclusions from
 805 products erupted by the Pavin's Group of Volcanoes, i.e., in the place of the most recent eruptive
 806 activity in the French Massif Central. Our results showed a progressive decrease (in time) of the
 807 pressure of magma storage (from more than 900 MPa down to 150-200 MPa) in parallel to magma

808 differentiation (from basanites at Montcineyre to benmoreites at Pavin). The geochemical analysis
809 of the noble gases entrapped in fluid inclusions led to two main conclusions. Firstly, Rc/Ra (6.5-
810 6.8) is in the range of ratios measured in fluid inclusions from mantle xenoliths in the Massif
811 Central (5.6±1.1, on average) in agreement with an origin from the Sub-Continental Lithospheric
812 Mantle (SCLM). Secondly, magma degassing ($^4\text{He}/^{40}\text{Ar}^*$ from 4.0 to 16.2) follows magma
813 differentiation and the progressive rise of the magma ponding zones. Based on these results, we
814 proposed an interpretative scheme of the evolution of the signature of noble gases and carbon
815 isotopes from mantle depth to crustal levels. Gas emissions currently emitted in the area (Rc/Ra =
816 6.1-6.7 and $^4\text{He}/^{40}\text{Ar}^* = 1.7$) point to an origin in the lithospheric mantle according to this model.
817 Meanwhile, an increase in Rc/Ra and in $^4\text{He}/^{40}\text{Ar}^*$ values in gaseous emissions is expected in the
818 case where a new batch of magma will rise from mantle depth to shallower levels. This inference
819 strongly encourages the establishment of an appropriate monitoring strategy of gaseous emissions in
820 the area focused on the time evolution of (1) noble gas ratios from local mineral springs and (2) soil
821 gas (CO_2 , Rn) emissions.

822

823 **Acknowledgments**

824 Part of the data were acquired in the frame of the Master thesis of G. Padeloup (Raman analysis of
825 fluid inclusions) at the Laboratoire Magmas et Volcans under the supervision of G. Boudoire, N.
826 Cluzel, F. Schiavi, and A.L. Rizzo. We thank C. Bosq, J.-L. Devidal, C. Fonquernie, and E. Voyer
827 at the LMV as well as M. Tantillo, M.G. Misseri, Y. Oliveri, and F. Salerno at the INGV for their
828 priceless support during sample preparation and gas analysis in laboratory. P. Boivin, D. Briot, E.
829 Médard, and C. Deniel are acknowledged for constructive discussions at the LMV. We thank S.
830 Niedermann and one anonymous reviewer for suggestions that greatly improved the manuscript.
831 Data discussed in this study are fully available in the Supporting Information. This research is part
832 of the PROVA² initiative held at the OPGC-LMV and has benefited from the Memorandum of
833 Understanding established between the UCA and the INGV. This research was financed by the
834 French Government Laboratory of Excellence initiative n° ANR-10-LABX-0006, the Region
835 Auvergne and the European Regional Development Fund through the project DegazRift. This is
836 Laboratory of Excellence ClerVolc contribution number XXX.

837

838 **References**

839

840 Aeschbach-Hertig, W., Hofer, M., Kipfer, R., Imboden, D. M., & Wieler, R. (1999). Accumulation of mantle gases in a
841 permanently stratified volcanic Lake (Lac Pavin, France). *Geochimica et Cosmochimica Acta*, 63(19-20), 3357-3372.

842

843 Arai, S. (1994). Characterization of spinel peridotites by olivine-spinel compositional relationships: review and
844 interpretation. *Chemical geology*, 113(3-4), 191-204.

845

846 Aubaud, C., Pineau, F., Hékinian, R., & Javoy, M. (2005). Degassing of CO_2 and H_2O in submarine lavas from the
847 Society hotspot. *Earth and Planetary Science Letters*, 235(3-4), 511-527.

848

849 Aubaud, C., Pineau, F., Jambon, A., & Javoy, M. (2004). Kinetic disequilibrium of C, He, Ar and carbon isotopes
850 during degassing of mid-ocean ridge basalts. *Earth and Planetary Science Letters*, 222(2), 391-406.

851

852 Babuška, V., Plomerová, J., Vecsey, L., Granet, M., & Achauer, U. (2002). Seismic anisotropy of the French Massif
853 Central and predisposition of Cenozoic rifting and volcanism by Variscan suture hidden in the mantle lithosphere.
854 *Tectonics*, 21(4), 11-1. <https://doi.org/10.1029/2001TC901035>.

855

856 Bakker, R. J. (2003). Package FLUIDS 1. Computer programs for analysis of fluid inclusion data and for modelling
857 bulk fluid properties. *Chemical Geology*, 194(1-3), 3-23.

858

859 Barry, P. H., Hilton, D. R., Fischer, T. P., De Moor, J. M., Mangasini, F., & Ramirez, C. (2013). Helium and carbon
860 isotope systematics of cold “mazuku” CO_2 vents and hydrothermal gases and fluids from Rungwe Volcanic Province,
861 southern Tanzania. *Chemical Geology*, 339, 141-156.

862

863 Battani, A., Deville, E., Faure, J. L., Jeandel, E., Noirez, S., Tocqué, E., ... & Bauer, A. (2010). Geochemical study of
864 natural CO₂ emissions in the French Massif Central: how to predict origin, processes and evolution of CO₂ leakage. *Oil*
865 *& Gas Science and Technology—Revue de l'Institut Français du Pétrole*, 65(4), 615-633.
866

867 Bilal, A., & Touret, J. (1977). Les inclusions fluides des phenocristaux des laves basaltiques du Puy Beaunit (Massif
868 Central Français). *Bulletin de Minéralogie*, 100(6), 324-328.
869

870 Boivin, P., Besson, J. C., Briot, D., Camus, G., De Goër de Hervé, A., Gourgaud, A., ... & Livet, M. (2017).
871 Volcanologie de la Chaîne des Puys. *Editions Du Parc Naturel Régional Des Volcans d'Auvergne*, 5th ed. ; IGN : San
872 Francisco, CA, USA.
873

874 Bonadiman, C., Coltorti, M., Beccaluva, L., Griffin, W. L., O'Reilly, S. Y., & Siena, F. (2011). Metasomatism versus
875 host magma infiltration: a case study of Sal mantle xenoliths, Cape Verde Archipelago. *Geol. Soc. Am. Spec. Pap*, 478,
876 283-305.
877

878 Boudoire, G., Calabrese, S., Colacicco, A., Sordini, P., Habakaramo Macumu, P., Rafflin, V., ... & Tedesco, D. (2022).
879 Scientific response to the 2021 eruption of Nyiragongo based on the implementation of a participatory monitoring
880 system. *Scientific reports*, 12(1), 1-10.
881

882 Boudoire, G., Di Muro, A., Michon, L., & Metrich, N. (2021). Footprints and conditions of multistep alkali enrichment
883 in basaltic melts at Piton de la Fournaise (La Réunion Island, Indian Ocean). *Bulletin of Volcanology*, 83(12), 1-31.
884

885 Boudoire, G., Rizzo, A. L., Di Muro, A., Grassa, F., & Liuzzo, M. (2018). Extensive CO₂ degassing in the upper mantle
886 beneath oceanic basaltic volcanoes: First insights from Piton de la Fournaise volcano (La Réunion Island). *Geochimica*
887 *et Cosmochimica Acta*, 235, 376-401.
888

889 Boulliang, J., & Wood, B. J. (2022). SO₂ solubility and degassing behavior in silicate melts. *Geochimica et*
890 *Cosmochimica Acta*, 336, 150-164.
891

892 Bräuer, K., Geissler, W. H., Kämpf, H., Niedermann, S., & Rman, N. (2016). Helium and carbon isotope signatures of
893 gas exhalations in the westernmost part of the Pannonian Basin (SE Austria/NE Slovenia): Evidence for active
894 lithospheric mantle degassing. *Chemical Geology*, 422, 60-70.
895

896 Bräuer, K., Kämpf, H., Koch, U., & Strauch, G. (2011). Monthly monitoring of gas and isotope compositions in the free
897 gas phase at degassing locations close to the Nový Kostel focal zone in the western Eger Rift Czech Republic. *Chemical*
898 *Geology*, 290(3-4), 163-176.
899

900 Bräuer, K., Kämpf, H., Niedermann, S., & Strauch, G. (2013). Indications for the existence of different magmatic
901 reservoirs beneath the Eifel area (Germany): A multi-isotope (C, N, He, Ne, Ar) approach. *Chemical Geology*, 356,
902 193-208.
903

904 Bräuer, K., Kämpf, H., Niedermann, S., & Wetzel, H. U. (2017). Regional distribution pattern of carbon and helium
905 isotopes from different volcanic fields in the French Massif Central: Evidence for active mantle degassing and water
906 transport. *Chemical Geology*, 469, 4-18.
907

908 Brousse, R., & Rudel, A. (1964). Bombes de péridotites, de norites, de charnockites et de granulites dans les scories du
909 Puy Beaunit. *Comptes-rendus de l'Académie des Sciences*, 259(1), 185.
910

911 Brown, S. K., Auker, M. R., & Sparks, R. S. J. (2015). Populations around Holocene volcanoes and development of a
912 Population Exposure Index. *Global volcanic hazards and risk*, 223-232.
913

914 Buikin, A., Trieloff, M., Hopp, J., Althaus, T., Korochantseva, E., Schwarz, W. H., & Altherr, R. (2005). Noble gas
915 isotopes suggest deep mantle plume source of late Cenozoic mafic alkaline volcanism in Europe. *Earth and Planetary*
916 *Science Letters*, 230(1-2), 143-162.
917

918 Burnard, P. (2004). Diffusive fractionation of noble gases and helium isotopes during mantle melting. *Earth and*
919 *Planetary Science Letters*, 220(3-4), 287-295.
920

921 Buso, R., Laporte, D., Schiavi, F., Cluzel, N., & Fonquernie, C. (2022). High-pressure homogenization of olivine-
922 hosted CO₂-rich melt inclusions in a piston cylinder: insight into the volatile content of primary mantle melts. *European*
923 *Journal of Mineralogy Special Volume: Experiments and Mineral Physics at mantle depths. European Journal of*
924 *Mineralogy*, 34, 325-349. <https://doi.org/10.5194/ejm-34-325-2022>.

925
926
927
928
929
930
931
932
933
934
935
936
937
938
939
940
941
942
943
944
945
946
947
948
949
950
951
952
953
954
955
956
957
958
959
960
961
962
963
964
965
966
967
968
969
970
971
972
973
974
975
976
977
978
979
980
981
982
983
984
985

Caracausi, A., Italiano, F., Paonita, A., Rizzo, A., & Nuccio, P. M. (2003). Evidence of deep magma degassing and ascent by geochemistry of peripheral gas emissions at Mount Etna (Italy): Assessment of the magmatic reservoir pressure. *Journal of Geophysical Research: Solid Earth*, 108(B10).

Chiodini, G., Paonita, A., Aiuppa, A., Costa, A., Caliro, S., De Martino, P., ... & Vandemeulebrouck, J. (2016). Magmas near the critical degassing pressure drive volcanic unrest towards a critical state. *Nature communications*, 7(1), 1-9.

Duan, Z., Møller, N., & Weare, J. H. (1992). An equation of state for the CH₄-CO₂-H₂O system: I. Pure systems from 0 to 1000 C and 0 to 8000 bar. *Geochimica et Cosmochimica Acta*, 56(7), 2605-2617.

Duan, Z., Møller, N., & Weare, J. H. (1996). A general equation of state for supercritical fluid mixtures and molecular dynamics simulation of mixture PVTX properties. *Geochimica et Cosmochimica Acta*, 60(7), 1209-1216.

Edmonds, M. (2008). New geochemical insights into volcanic degassing. *Philosophical Transactions of the Royal Society A: Mathematical, Physical and Engineering Sciences*, 366(1885), 4559-4579.

Eguchi, J., & Dasgupta, R. (2018). A CO₂ solubility model for silicate melts from fluid saturation to graphite or diamond saturation. *Chemical Geology*, 487, 23-38.

Fall, A., Tattitch, B., & Bodnar, R. J. (2011). Combined microthermometric and Raman spectroscopic technique to determine the salinity of H₂O-CO₂-NaCl fluid inclusions based on clathrate melting. *Geochimica et Cosmochimica Acta*, 75(4), 951-964.

Féménias, O., Coussaert, N., Berger, J., Mercier, J. C. C., & Demaiffe, D. (2004). Metasomatism and melting history of a Variscan lithospheric mantle domain: evidence from the Puy Beaunit xenoliths (French Massif Central). *Contributions to Mineralogy and Petrology*, 148(1), 13-28.

Féménias, O., Mercier, J. C. C., & Demaiffe, D. (2001). Pétrologie des xénolites ultramafiques du puy Beaunit (Massif central français): un gisement atypique du manteau sous-continentale. *Comptes Rendus de l'Académie des Sciences-Series IIA-Earth and Planetary Science*, 332(9), 535-542.

France, L., Demacon, M., Gurenko, A. A., & Briot, D. (2016). Oxygen isotopes reveal crustal contamination and a large, still partially molten magma chamber in Chaîne des Puys (French Massif Central). *Lithos*, 260, 328-338.

Frezzotti, M. L., Tecce, F., & Casagli, A. (2012). Raman spectroscopy for fluid inclusion analysis. *Journal of Geochemical Exploration*, 112, 1-20.

Frezzotti, M. L., & Touret, J. L. (2014). CO₂, carbonate-rich melts, and brines in the mantle. *Geoscience Frontiers*, 5(5), 697-710.

Gal, F., & Gadalia, A. (2011). Soil gas measurements around the most recent volcanic system of metropolitan France (Lake Pavin, Massif Central). *Comptes Rendus Geoscience*, 343(1), 43-54.

Gal, F., Leconte, S., & Gadalia, A. (2018). The "Escarot" gas seep, French Massif Central: CO₂ discharge from a quiescent volcanic system—characterization and quantification of gas emissions. *Journal of Volcanology and Geothermal Research*, 353, 68-82.

Gautheron, C., & Moreira, M. (2002). Helium signature of the subcontinental lithospheric mantle. *Earth and Planetary Science Letters*, 199(1-2), 39-47.

Gautheron, C., Moreira, M., & Allègre, C. (2005). He, Ne and Ar composition of the European lithospheric mantle. *Chemical Geology*, 217(1-2), 97-112.

Graham, D. W., Jenkins, W. J., Kurz, M. D., & Batiza, R. (1987). Helium isotope disequilibrium and geochronology of glassy submarine basalts. *Nature*, 326(6111), 384-386.

Hagiwara, Y., Yoshida, K., Yoneda, A., Torimoto, J., & Yamamoto, J. (2021a). Experimental variable effects on laser heating of inclusions during Raman spectroscopic analysis. *Chemical Geology*, 559, 119928.

986 Hagiwara, Y., Kawano, T., Takahata, K., Torimoto, J., & Yamamoto, J. (2021b). Temperature dependence of a Raman
987 CO₂ densimeter from 23° C to 200° C and 7.2 to 248.7 MPa: Evaluation of density underestimation by laser
988 heating. *Journal of Raman Spectroscopy*, 52(10), 1744-1757.
989
990 Hansteen, T. H., & Klügel, A. (2008). Fluid inclusion thermobarometry as a tracer for magmatic processes. *Reviews in
991 Mineralogy and Geochemistry*, 69(1), 143-177.
992
993 Hensch, M., Dahm, T., Ritter, J., Heimann, S., Schmidt, B., Stange, S., & Lehmann, K. (2019). Deep low-frequency
994 earthquakes reveal ongoing magmatic recharge beneath Laacher See Volcano (Eifel, Germany). *Geophysical Journal
995 International*, 216(3), 2025-2036.
996
997 Hildner, E., Klügel, A., & Hauff, F. (2011). Magma storage and ascent during the 1995 eruption of Fogo, Cape Verde
998 Archipelago. *Contributions to Mineralogy and Petrology*, 162(4), 751-772.
999
1000 Hoefs, J. (1997). *Stable isotope geochemistry* (Vol. 201). Berlin: Springer.
1001
1002 Iacono-Marziano, G., Paonita, A., Rizzo, A., Scaillet, B., & Gaillard, F. (2010). Noble gas solubilities in silicate melts:
1003 new experimental results and a comprehensive model of the effects of liquid composition, temperature, and
1004 pressure. *Chemical Geology*, 279(3-4), 145-157.
1005
1006 Jambon, A., Weber, H., & Braun, O. (1986). Solubility of He, Ne, Ar, Kr and Xe in a basalt melt in the range 1250–
1007 1600 °C. Geochemical implications. *Geochimica et Cosmochimica Acta*, 50(3), 401-408.
1008
1009 Jannot S., Schiano P. & Boivin P. (2005). Melt inclusions in scoria and associated mantle xenoliths of Puy Beaunit
1010 Volcano, Chaîne des Puys, Massif Central, France. *Contributions to Mineralogy and Petrology*, 149, 600-612.
1011
1012 Javoy, M., Pineau, F., & Iiyama, I. (1978). Experimental determination of the isotopic fractionation between gaseous
1013 CO₂ and carbon dissolved in tholeiitic magma. *Contributions to Mineralogy and Petrology*, 67(1), 35-39.
1014
1015 Jennings, E. S., Gibson, S. A., Maclennan, J., & Heinonen, J. S. (2017). Deep mixing of mantle melts beneath
1016 continental flood basalt provinces: Constraints from olivine-hosted melt inclusions in primitive magmas. *Geochimica et
1017 Cosmochimica Acta*, 196, 36-57.
1018
1019 Jézéquel, D., Michard, G., Viollier, E., Agrinier, P., Albéric, P., Lopes, F., ... & Bergonzini, L. (2016). Carbon cycle in
1020 a meromictic crater lake: Lake Pavin, France. In *Lake Pavin* (pp. 185-203). Springer, Cham.
1021
1022 Juvigné, E., & Miallier, D. (2016). Distribution, tephrostratigraphy and chronostratigraphy of the widespread eruptive
1023 products of Pavin volcano. In *Lake Pavin* (pp. 143-154). Springer, Cham.
1024
1025 Klügel, A., Day, S., Schmid, M., & Faria, B. (2020). Magma plumbing during the 2014–2015 eruption of Fogo (Cape
1026 Verde Islands). *Frontiers in Earth Science*, 8, 157.
1027
1028 Kobayashi, T., Yamamoto, J., Hirajima, T., Ishibashi, H., Hirano, N., Lai, Y., ... & Arai, S. (2012). Conformity and
1029 precision of CO₂ densimetry in CO₂ inclusions: Microthermometry versus Raman microspectroscopic densimetry.
1030 *Journal of Raman Spectroscopy*, 43(8), 1126-1133.
1031
1032 Kreemer, C., Blewitt, G., & Davis, P. M. (2020). Geodetic evidence for a buoyant mantle plume beneath the Eifel
1033 volcanic area, NW Europe. *Geophysical Journal International*, 222(2), 1316-1332.
1034
1035 Kurz, M. D., Kenna, T. C., Lassiter, J. C., & DePaolo, D. J. (1996). Helium isotopic evolution of Mauna Kea volcano:
1036 First results from the 1- km drill core. *Journal of Geophysical Research: Solid Earth*, 101(B5), 11781-11791.
1037
1038 Lamadrid, H. M., Moore, L. R., Moncada, D., Rimstidt, J. D., Burruss, R. C., & Bodnar, R. J. (2017). Reassessment of
1039 the Raman CO₂ densimeter. *Chemical Geology*, 450, 210-222.
1040
1041 Lange, R. L., & Carmichael, I. S. (1990). Thermodynamic properties of silicate liquids with emphasis on density,
1042 thermal expansion and compressibility. *Reviews in Mineralogy and Geochemistry*, 24(1), 25-64.
1043
1044 Leake, B. E., Woolley, A. R., Arps, C. E., Birch, W. D., Gilbert, M. C., Grice, J. D., ... & Youzhi, G. (1997).
1045 Nomenclature of amphiboles; report of the Subcommittee on Amphiboles of the International Mineralogical
1046 Association Commission on new minerals and mineral names. *Mineralogical magazine*, 61(405), 295-310.
1047

1048 Lee, J.-Y., Marti, K., Severinghaus, J. P., Kawamura, K., Yoo, H.-S., Lee, J. B., Kim, J. S. (2006). A Redetermination
1049 of the Isotopic Abundances of Atmospheric Ar. *Geochimica et Cosmochimica Acta*, 70, 4507–4512.
1050
1051 Lenoir, X., Garrido, C. J., Bodinier, J. L., & Dautria, J. M. (2000). Contrasting lithospheric mantle domains beneath the
1052 Massif Central (France) revealed by geochemistry of peridotite xenoliths. *Earth and Planetary Science Letters*, 181(3),
1053 359-375.
1054
1055 Longpré, M. A., Stix, J., Klügel, A., & Shimizu, N. (2017). Mantle to surface degassing of carbon-and sulphur-rich
1056 alkaline magma at El Hierro, Canary Islands. *Earth and Planetary Science Letters*, 460, 268-280.
1057
1058 Lustrino, M., & Wilson, M. (2007). The circum-Mediterranean anorogenic Cenozoic igneous province. *Earth-Science*
1059 *Reviews*, 81(1-2), 1-65.
1060
1061 Martel, C., Champallier, R., Prouteau, G., Pichavant, M., Arbaret, L., Balcone-Boissard, H., ... & Scaillet, B. (2013).
1062 Trachyte phase relations and implication for magma storage conditions in the Chaîne des Puys (French Massif
1063 Central). *Journal of Petrology*, 54(6), 1071-1107.
1064
1065 Matthews, A., Fouillac, C., Hill, R., O'Nions, R. K., & Oxburgh, E. R. (1987). Mantle-derived volatiles in continental
1066 crust: the Massif Central of France. *Earth and Planetary Science Letters*, 85(1-3), 117-128.
1067
1068 Matusiak-Małek, M., Puziewicz, J., Ntaflos, T., Grégoire, M., Kukuła, A., & Wojtulek, P. M. (2017). Origin and
1069 evolution of rare amphibole-bearing mantle peridotites from Wilcza Góra (SW Poland), Central Europe. *Lithos*, 286,
1070 302-323.
1071
1072 Merle, O., & Michon, L. (2001). The formation of the West European Rift; a new model as exemplified by the Massif
1073 Central area. *Bulletin de la Société géologique de France*, 172(2), 213-221.
1074
1075 Michard, G., Viollier, E., Jézéquel, D., & Sarazin, G. (1994). Geochemical study of a crater lake: Pavin Lake, France -
1076 Identification, location and quantification of the chemical reactions in the lake. *Chemical Geology*, 115(1-2), 103-115.
1077
1078 Michon, L., & Merle, O. (2001). The evolution of the Massif Central Rift; spatio-temporal distribution of the
1079 volcanism. *Bulletin de la Société géologique de France*, 172(2), 201-211.
1080
1081 Mook, W. G., Bommerson, J. C., & Staverman, W. H. (1974). Carbon isotope fractionation between dissolved
1082 bicarbonate and gaseous carbon dioxide. *Earth and planetary science letters*, 22(2), 169-176.
1083
1084 Moreira, M. (2013). Noble gas constraints on the origin and evolution of Earth's volatiles. *Geochemical*
1085 *Perspectives*, 2(2), 229-230.
1086
1087 Moreira, M., Rouchon, V., Muller, E., & Noirez, S. (2018). The xenon isotopic signature of the mantle beneath Massif
1088 Central. *Geochem. Perspect. Lett.*, 6, 28-32.
1089
1090 Nomade, S., Genty, D., Sasco, R., Scao, V., Féruglio, V., Baffier, D., ... & Geneste, J. M. (2016). A 36,000-year-old
1091 volcanic eruption depicted in the Chauvet-Pont d'Arc Cave (Ardèche, France)? *PLoS One*, 11(1), e0146621.
1092
1093 Olive, P., & Boulègue, J. (2004). Étude biogéochimique d'un lac méromictique: le lac Pavin, France/Biogeochemical
1094 study of a meromictic lake: Pavin lake, France. *Géomorphologie: relief, processus, environnement*, 10(4), 305-316.
1095
1096 Oppenheimer, C. (2015). Eruption politics. *Nature Geoscience*, 8(4), 244-245.
1097
1098 Ozima, M., & Podosek, F. A. (2002). Noble gas geochemistry. Cambridge University Press.
1099
1100 Paonita, A., Caracausi, A., Iacono-Marziano, G., Martelli, M., & Rizzo, A. (2012). Geochemical evidence for mixing
1101 between fluids exsolved at different depths in the magmatic system of Mt Etna (Italy). *Geochimica et Cosmochimica*
1102 *Acta*, 84, 380-394.
1103
1104 Pilet S. (2015). Generation of low-silica alkaline lavas: Petrological constraints, models, and thermal implications. In
1105 Foulger G. R., Lustrino M., and King S. D., eds., *The Interdisciplinary Earth: A Volume in Honor of Don L. Anderson*.
1106 Geological Society of America Special Paper 514 and American Geophysical Union Special Publication 71: 281-304.
1107

1108 Putirka, K. D. (2008). Thermometers and barometers for volcanic systems. *Reviews in mineralogy and*
1109 *geochemistry*, 69(1), 61-120.

1110

1111 Rizzo, A. L., Faccini, B., Casetta, F., Faccincani, L., Ntaflos, T., Italiano, F., & Coltorti, M. (2021). Melting and
1112 metasomatism in West Eifel and Siebengebirge Sub-Continental Lithospheric Mantle: Evidence from concentrations of
1113 volatiles in fluid inclusions and petrology of ultramafic xenoliths. *Chemical Geology*, 581, 120400.

1114

1115 Rizzo, A. L., Pelorosso, B., Coltorti, M., Ntaflos, T., Bonadiman, C., Matusiak-Małek, M., ... & Bergonzoni, G. (2018).
1116 Geochemistry of noble gases and CO₂ in fluid inclusions from lithospheric mantle beneath Wilcza Góra (Lower Silesia,
1117 southwest Poland). *Frontiers in Earth Science*, 6, 215.

1118

1119 Roedder, E. (1984). Volume 12: fluid inclusions. *Reviews in mineralogy*, 12, 644.

1120

1121 Rondet, M., Martel, C., & Bourdier, J. L. (2019). The intermediate step in fractionation trends of mildly alkaline
1122 volcanic suites: An experimental insight from the Pavin trachyandesite (Massif Central, France). *Comptes Rendus*
1123 *Geoscience*, 351(8), 525-539.

1124

1125 Sandoval-Velasquez, A., Rizzo, A. L., Aiuppa, A., Straub, S. M., Gomez-Tuena, A., & Espinasa-Perena, R. (2022). The
1126 heterogeneity of the Mexican lithospheric mantle: Clues from noble gas and CO₂ isotopes in fluid inclusions. *Frontiers*
1127 *in Earth Science*.

1128

1129 Sano, Y., & Marty, B. (1995). Origin of carbon in fumarolic gas from island arcs. *Chemical Geology*, 119(1-4), 265-
1130 274.

1131

1132 Schiavi, F., Bolfan-Casanova, N., Buso, R., Laumonier, M., Laporte, D., Medjoubi, K., Venugopal, S., Gómez-Ulla, A.,
1133 Cluzel, N., & Hardiagon, M. (2020). Quantifying magmatic volatiles by Raman microtomography of glass inclusion-
1134 hosted bubbles. *Geochemical Perspectives Letters*, 16, 17-24.

1135

1136 Shaw, A. M., Hilton, D. R., Macpherson, C. G., & Sinton, J. M. (2004). The CO₂-He-Ar-H₂O systematics of the Manus
1137 back-arc basin: Resolving source composition from degassing and contamination effects. *Geochimica et Cosmochimica*
1138 *Acta*, 68(8), 1837-1855.

1139

1140 Shoji, S., & Takahashi, T. (2002). Environmental and agricultural significance of volcanic ash soils. *Global*
1141 *Environmental Research - English Edition*, 6(2), 113-135.

1142

1143 Song, Y., Chou, I. M., Hu, W., Robert, B., & Lu, W. (2009). CO₂ density- Raman shift relation derived from synthetic
1144 inclusions in fused silica capillaries and its application. *Acta Geologica Sinica - English Edition*, 83(5), 932-938.

1145

1146 Spilliaert, N., Allard, P., Métrich, N., & Sobolev, A. V. (2006). Melt inclusion record of the conditions of ascent,
1147 degassing, and extrusion of volatile- rich alkali basalt during the powerful 2002 flank eruption of Mount Etna
1148 (Italy). *Journal of Geophysical Research: Solid Earth*, 111(B4).

1149

1150 Spooner, C., Scheck-Wenderoth, M., Götze, H. J., Ebbing, J., Hetényi, G., & AlpArray Working Group. (2019).
1151 Density distribution across the Alpine lithosphere constrained by 3-D gravity modelling and relation to seismicity and
1152 deformation. *Solid Earth*, 10(6), 2073-2088.

1153

1154 Streckeisen, A. (1974). Classification and nomenclature of plutonic rocks recommendations of the IUGS
1155 subcommission on the systematics of igneous rocks. *Geologische Rundschau*, 63(2), 773-786.

1156

1157 Sublett Jr, D. M., Sendula, E., Lamadrid, H., Steele- MacInnis, M., Spiekermann, G., Burruss, R. C., & Bodnar, R. J.
1158 (2020). Shift in the Raman symmetric stretching band of N₂, CO₂, and CH₄ as a function of temperature, pressure, and
1159 density. *Journal of Raman Spectroscopy*, 51(3), 555-568.

1160

1161 Trull, T. W., & Kurz, M. D. (1993). Experimental measurements of ³He and ⁴He mobility in olivine and clinopyroxene
1162 at magmatic temperatures. *Geochimica et cosmochimica acta*, 57(6), 1313-1324.

1163

1164 Uenver-Thiele, L., Woodland, A. B., Downes, H., & Altherr, R. (2014). Oxidation state of the lithospheric mantle
1165 below the Massif Central, France. *Journal of Petrology*, 55(12), 2457-2480.

1166

1167 Uenver-Thiele, L., Woodland, A. B., Seitz, H. M., Downes, H., & Altherr, R. (2017). Metasomatic processes revealed
1168 by trace element and redox signatures of the lithospheric mantle beneath the Massif Central, France. *Journal of*
1169 *Petrology*, 58(3), 395-422.

1170
1171 Ulrych, J., Pivec, E., Lang, M., Balogh, K., & Kropáček, V. (1999). Cenozoic intraplate volcanic rock series of the
1172 Bohemian Massif: a review. *Geolines*, 9, 123-129.

1173
1174 Upton, B. G. J., Downes, H., Kirstein, L. A., Bonadiman, C., Hill, P. G., & Ntaflos, T. (2011). The lithospheric mantle
1175 and lower crust–mantle relationships under Scotland: a xenolithic perspective. *Journal of the Geological*
1176 *Society*, 168(4), 873-886.

1177
1178 Van den Kerkhof, A. M., & Olsen, S. N. (1990). A natural example of superdense CO₂ inclusions: microthermometry
1179 and Raman analysis. *Geochimica et Cosmochimica Acta*, 54(3), 895-901.

1180
1181 Venugopal, S., Schiavi, F., Moune, S., Bolfan-Casanova, N., Druitt, T., & Williams-Jones, G. (2020). Melt inclusion
1182 vapour bubbles: the hidden reservoir for major and volatile elements. *Scientific Reports*, 10(1), 1-14.

1183
1184 Villemant, B., Caron, B., Thierry, P., & Boivin, P. (2016). Magmatic Evolution of Pavin's Group of Volcanoes:
1185 Petrology, Geochemistry and Modeling of Differentiation Processes. A Preliminary Study. In *Lake Pavin* (pp. 129-142).
1186 Springer.

1187
1188 Wanamaker, B. J., & Evans, B. (1989). Mechanical re-equilibration of fluid inclusions in San Carlos olivine by power-
1189 law creep. *Contributions to Mineralogy and Petrology*, 102(1), 102-111.

1190
1191 Wang, X., Chou, I. M., Hu, W., Burruss, R. C., Sun, Q., & Song, Y. (2011). Raman spectroscopic measurements of CO₂
1192 density: Experimental calibration with high-pressure optical cell (HPOC) and fused silica capillary capsule (FSCC) with
1193 application to fluid inclusion observations. *Geochimica et Cosmochimica Acta*, 75(14), 4080-4093.

1194
1195 Yamamoto, J., Nishimura, K., Sugimoto, T., Takemura, K., Takahata, N., & Sano, Y. (2009). Diffusive fractionation of
1196 noble gases in mantle with magma channels: origin of low He/Ar in mantle-derived rocks. *Earth and Planetary Science*
1197 *Letters*, 280(1-4), 167-174.

1198
1199 Zanon, V., & Frezzotti, M. L. (2013). Magma storage and ascent conditions beneath Pico and Faial islands (Azores
1200 archipelago): A study on fluid inclusions. *Geochemistry, Geophysics, Geosystems*, 14(9), 3494-3514.

1201
1202
1203
1204
1205
1206
1207
1208
1209
1210
1211
1212
1213
1214
1215
1216
1217
1218
1219
1220
1221
1222

1223
 1224
 1225
 1226
 1227

Tables

Δ Mg-number between core and rim	Olivine					Clinopyroxene				
	n	Min	Max	Average	σ	n	Min	Max	Average	σ
<u>Pavin's Group of Volcanoes</u>										
Montcineyre	4	-3.6	0.4	-1.1	1.9	8	-2.4	7.6	0.8	3.5
Montchal	4	0.3	3.3	1.4	1.3	10	-7.0	6.8	0.1	4.8
Pavin	8	-0.9	4.2	0.4	1.6	9	-1.3	3.0	1.2	1.4
<u>Puy Beaunit</u>										
Harzburgite	5	-0.5	0.1	-0.1	0.2	10	-0.7	1.1	0.4	0.6
Lherzolute	5	-0.5	0.0	-0.3	0.2	10	-0.5	1.0	0.4	0.4

1228
 1229
 1230
 1231
 1232
 1233
 1234

Table 1. Difference between the Mg-number calculated for the core and the rim of each single crystal of olivine and clinopyroxene from mantle enclaves (Puy Beaunit) and lapilli and pumices (Pavin’s Group of Volcanoes). Negative value denotes a reverse zoning whereas positive value highlights a normal zoning. Note that zoning patterns of clinopyroxene crystals revealed by Backscattered electrons (BSE) imagery during EPMA analyses appear much more complex than simple normal or reverse zoning and would deserve a dedicated focus that is not the scope of the present study. ‘n’ denotes the number of crystals where the pair core-rim was analysed.

Host mineral	Group	Type	Shape	Trapping	n	Fermi dyad split Δ (cm ⁻¹)				CO ₂ -H ₂ O mixture density ρ (g/cm ³)				Other phases	
						Min	Max	Average	σ	Min	Max	Average	σ		
<u>Pavin's Group of Volcanoes</u>															
Montcineyre	Olivine	F5	Secondary	Rounded	Homogenous	8	104.69	105.07	104.79	0.13	0.89	1.04	0.94	0.05	SO ₂ - Carbonate - Sulphide
	Olivine	F3	Secondary	Rounded	Heterogenous	5	104.64	104.97	104.85	0.15	0.88	1.00	0.96	0.06	Carbonate
	Olivine	F1	Primary	Negatively shaped	Homogenous	2	104.99	105.00	104.99	0.00	1.01	1.01	1.01	0.00	SO ₂
	Clinopyroxene	F3	Secondary	Rounded	Homogenous	9	104.53	104.80	104.66	0.11	0.83	0.94	0.88	0.04	
Montchal	Olivine	F2	Pseudo-Secondary	Rounded	Homogenous	1	104.58	104.58	104.58	0.00	0.85	0.85	0.85	0.00	Carbonate
	Olivine	F4	Primary	Rounded	Heterogenous	1	104.72	104.72	104.72	0.00	0.91	0.91	0.91	0.00	-
Pavin	Olivine	F3	Secondary	Rounded	Homogenous	3	104.80	104.90	104.85	0.05	0.94	0.98	0.96	0.02	
<u>Puy Beaunit</u>															
Harzburgite	Orthopyroxene	f3	Secondary	Rounded	Homogenous	4	104.21	104.89	104.70	0.33	0.69	0.97	0.90	0.14	SO ₂
	Clinopyroxene	f3	Secondary	Rounded	Homogenous	4	102.92	103.03	102.97	0.04	0.10	0.15	0.13	0.02	Carbonate - Sulphate
	Olivine	f2	Secondary	Necking	Homogenous	8	104.01	104.45	104.36	0.15	0.60	0.80	0.76	0.06	SO ₂
	Olivine	f4	Secondary	Rounded	Homogenous	4	104.73	104.75	104.74	0.01	0.91	0.92	0.91	0.00	SO ₂
Lherzolute	Orthopyroxene	f3	Secondary	Rounded	Heterogenous	8	103.48	104.85	103.84	0.61	0.36	0.96	0.52	0.27	Sulphate
	Clinopyroxene	f3	Secondary	Rounded	Homogenous	2	102.86	102.92	102.89	0.04	0.08	0.10	0.09	0.02	Sulphate
	Clinopyroxene	f1	Secondary	Negatively shaped	Homogenous	11	104.80	104.98	104.90	0.06	0.94	1.01	0.98	0.02	-

Table 2. Number of analysed fluid inclusions (n), Fermi dyad split (Δ), CO₂ density (ρ) (by considering the presence of a CO₂-H₂O initial mixture), and secondary phases detected by Raman spectroscopy for each family of fluid inclusions (F1-F5 for the Pavin's Group of Volcanoes and f1-f4 for Puy Beaunit; see text for explanation). Max: maximum. Min: minimum. Av: average. The standard deviation (σ) on the average was also calculated.

1240

	Absolute Gas Contents (mol/g)											Ratio							Carbon isotopy		
	Gas	⁴ He	³ He	²⁰ Ne	⁴⁰ Ar	³⁸ Ar	³⁶ Ar	⁴⁰ Ar*	CO ₂	N ₂	⁴ He/ ²⁰ Ne	⁴ He/ ⁴⁰ Ar*	⁴ He/CO ₂	R/Ra	Rc/Ra	2σ	⁴⁰ Ar/ ³⁶ Ar	CO ₂ / ³ He	CO ₂ (mol/g)	δ ¹³ C (‰)	
	10 ⁻⁹	10 ⁻¹³	10 ⁻¹⁸	10 ⁻¹⁶	10 ⁻¹³	10 ⁻¹⁶	10 ⁻¹⁵	10 ⁻¹³	10 ⁻⁹	10 ⁻¹⁰	10 ⁻⁴							10 ⁸		10 ⁻⁸	
<u>Pavin's Group of Volcanoes</u>																					
Montcineyre	OI	6.44	20.3	19.3	3.63	13.4	5.17	2.80	5.11	5.89	5.23	5603	3.98	3.45	6.82	6.82	0.14	486	3.05		
Montchal	OI	1.61	12.0	11.1	18.2	16.4	9.32	5.14	1.22	1.16	4.14	657	9.82	10.3	6.63	6.63	0.16	325	1.05		
Pavin	Am	3.84	11.6	10.5	32.2	4.63	2.49	1.32	0.72	3.28	5.48	361	16.17	3.54	6.49	6.50	0.18	356	3.12		
<u>Puy Beaunit</u>																					
Harzburgite	OI	1.33	4.63	4.33	76.5	34.0	18.8	10.5	3.11	0.95	3.04	60	1.49	4.87	6.71	6.75	0.22	331	2.19		
	Opx	12.7	15.1	14.7	18.8	23.4	4.37	2.38	16.4	11.7	9.76	802	0.92	1.29	7.00	7.00	0.18	1001	7.91	1.06	-5.8
Lherzolite	OI	2.33	7.37	6.81	46.1	26.9	9.68	5.41	10.9	1.06	12.3	160	0.67	6.94	6.62	6.63	0.32	507	1.56		
	Opx	138	35	33	50	130	8.79	4.83	116	135	34.4	705	0.30	0.26	6.84	6.84	0.16	2735	40.4	10.3	-2.9

Table 3. Analysis of gas abundance, noble gases, and carbon isotopy (δ¹³C) of CO₂ released by crystal crushing. OI: olivine. Am: amphibole. Opx: orthopyroxene.

1241
1242
1243
1244
1245
1246
1247
1248
1249
1250
1251
1252
1253
1254
1255

	$^{40}\text{Ar}/^{36}\text{Ar}$	σ	$^{38}\text{Ar}/^{36}\text{Ar}$	σ	$^4\text{He}/^{20}\text{Ne}$	R/Ra	Rc/Ra	σ	$^4\text{He}/^{40}\text{Ar}^*$	$\text{CO}_2/{}^3\text{He}$	$^4\text{He}/\text{CO}_2$	$\delta^{13}\text{C}$ (‰)
Lac Pavin -70m	296.2	0.06	0.1880	0.0001	10.7	6.55	6.72	0.04		1.31E+09	8.09E-05	0.8
Lac Pavin -90m	296.0	0.05	0.1882	0.0001	4.1	6.02	6.45	0.04		2.07E+09	5.34E-05	-2.8
Escarot	407.2	0.13	0.1862	0.0003	921	6.07	6.07	0.03	1.73	5.25E+09	2.24E-05	-3.4

Table 4. Analysis of noble gases and carbon isotopy ($\delta^{13}\text{C}$) of CO_2 in natural gas emissions in the area of study (see Fig. 1).

1256
1257
1258
1259
1260
1261
1262
1263
1264
1265
1266
1267
1268
1269
1270
1271
1272
1273
1274
1275
1276
1277
1278
1279
1280
1281

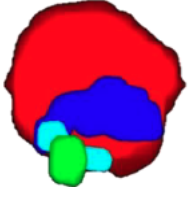
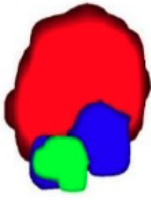
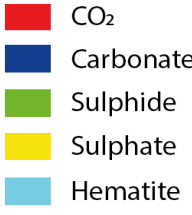
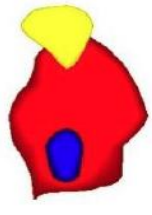
	Montcineyre			Lherzolite
	FI1	FI2	FI3	FIa
				
Measured CO₂ density				
ρ (g/cm ³)	0.88	0.92	1.00	0.14
Volume				
Spherical Volume (μm^3)	825	332	22	17
Max. Error on Volume (μm^3)	41	15	-	3
Volumetric distribution of the phases				
CO ₂ (% volume)	86	86	100	79
Carbonate (% volume)	10	11	-	6
Sulphide (% volume)	2	3	-	-
Sulphate (% volume)	-	-	-	15
Hematite (% volume)	2	-	-	-
Mass of CO₂ and carbonates				
CO ₂ (g)	(5.94-6.56)E-10	(2.52-2.76)E-10	2.24E-11	(1.43-2.26)E-12
Carbonate (g)	(1.15-1.32)E-10	(5.08-5.80)E-11	-	(1.01-1.87)E-12
Recalculated initial CO₂ density				
ρ (Initial CO ₂) (g/cm ³)	1.06	1.12	1.00	0.26
σ (g/cm ³)	0.09	0.07	-	0.09

Table 5. Reconstruction of the initial CO₂ density in some fluid inclusions characterised by the presence of carbonate. ρ is the measured CO₂ density used in this reconstruction (see Methods).

1289 **Supplementary material**

1290

1291 **Appendix 1.** Composition of the crystals analysed in this study

1292

1293 **Appendix 2.** Composition and CO₂ densimetry of the fluid inclusions

1294

1295 **Appendix 3.** Initial conditions used for the BED and FED modelling.

1296

1297